

# FUNCTIONAL MRI OF SKELETAL MUSCLE

*“It never gets easier, you just go faster.”*

– Greg LeMond

OPTIMIZATION OF FUNCTIONAL MAGNETIC RESONANCE  
IMAGING OF SKELETAL MUSCLE

BY

ANDREW D. DAVIS, B.Sc.

A THESIS

SUBMITTED TO THE DEPARTMENT OF  
MEDICAL PHYSICS & APPLIED RADIATION SCIENCES

AND THE SCHOOL OF GRADUATE STUDIES

OF MCMASTER UNIVERSITY

IN PARTIAL FULFILMENT OF THE REQUIREMENTS

FOR THE DEGREE OF

MASTER OF SCIENCE

© Copyright by Andrew D. Davis, December 2009

All Rights Reserved

Master of Science (2009)  
(Medical Physics & Applied Radiation Sciences)

McMaster University  
Hamilton, Ontario, Canada

TITLE: Optimization of Functional Magnetic Resonance Imaging  
of Skeletal Muscle

AUTHOR: Andrew D. Davis  
B.Sc. (Honours, Physics), Brock University, Canada

SUPERVISOR: Michael D. Noseworthy, Ph.D.

NUMBER OF PAGES: xii, 82

# Abstract

Peripheral vascular disease (PVD) is characterized by reduced blood flow to the lower limbs. Currently, the available tests for PVD either do not adequately characterize disease stage or do not provide adequate spatial information. The magnetic resonance imaging (MRI) method of blood oxygenation level dependent (BOLD) imaging is proposed because it is sensitive to local variations in metabolism, blood flow, and blood volume. Furthermore, MRI is non-invasive and can be repeated following intervention.

Exercise was used to modulate the BOLD signal because of its relevance to sufferers of claudication. Although BOLD imaging has been applied to muscle following brief contractions, the work presented in this thesis involved muscle imaging during sustained isometric plantar flexion. It was determined that motion may mask or mimic physiologically driven BOLD signal changes, even with apparently successful motion correction.

To minimize motion confounds and standardize the plantar flexion force, an MRI compatible ergometer was designed and constructed in-house. Next, a comparison study was made between raster (echo planar imaging; EPI) and spiral k-space trajectories. Though the EPI technique suffered from slight geometric distortion, it was found to be superior to spiral for imaging the lower leg, producing more consistent, sharper images with improved time resolution and signal to noise ratio (SNR). The SNR of EPI was  $70 \pm 30$  compared to spiral with  $17 \pm 6$ .

To aid with interpretation of BOLD signal changes, a flow sensitive alternating inversion recovery (FAIR) arterial spin labelling (ASL) sequence was used to assess perfusion during exercise. Image artifacts due to magnetic field inhomogeneity precluded the successful application of this sequence in the lower leg.

For future studies it is recommended that an eight receiver-channel radio frequency coil be used to improve SNR, and higher order shims be applied to improve  $B_0$  homogeneity. Lastly, a different ASL variant may improve perfusion results.

# Acknowledgements

This thesis would not have been completed without the support of my wife, Mollie, and my parents, Jack and Claire. Many thanks are also due to my supervisor, Dr. Michael Noseworthy, for his endless ideas and patient editing. Dr. Dinesh Kumbhare and Dr. Greg Wells were helpful with their physiological knowledge. Dr. Bareket Falk deserves many thanks for her helpful advice on study design and academic life. Raffy Dotan must be acknowledged for his superbly designed and built ergometer. The technologists of the Imaging Research Centre, especially Cheryl Contant and Julie Lecomte, are thanked for their help and advice.

Finally, Graeme Wardlaw, Adrian Koziak, Dr. Mohammed Ali Warsi, Brendan Boyd, Sergei Obruchkov, Peter Sheffield, Ali Fatemi, Dr. Reza Heydarian, Alyaa Elzibak, Oi Lei Wong, Paul Polak, Dr. Jeff Fortuna, Gavin Jones, Arv Jega, and Alex Weber are thanked for useful distractions.

# Contents

<b>Abstract</b>	<b>iii</b>
<b>Acknowledgements</b>	<b>iv</b>
<b>Contents</b>	<b>v</b>
<b>List of Figures</b>	<b>viii</b>
<b>List of Tables</b>	<b>ix</b>
<b>Symbols and Acronyms</b>	<b>x</b>
<b>1 Introduction</b>	<b>1</b>
1.1 Skeletal muscle . . . . .	1
1.1.1 Muscle anatomy . . . . .	1
1.1.2 Muscle function . . . . .	2
1.1.3 Muscle fibre types . . . . .	3
1.1.4 Muscles of the lower leg . . . . .	3
1.2 Peripheral vascular disease . . . . .	4
1.2.1 Testing for PVD . . . . .	5
<b>2 Magnetic resonance imaging</b>	<b>7</b>
2.1 Signal generation . . . . .	7
2.1.1 Spatial localization . . . . .	8
2.1.2 K-space . . . . .	9
2.2 Signal recovery and imaging parameters . . . . .	10
2.3 Gradient echo pulse sequence . . . . .	11
2.4 Fast acquisition techniques . . . . .	12
2.4.1 Echo planar imaging . . . . .	13
2.4.2 Spiral imaging . . . . .	15
2.5 Blood oxygenation level dependant imaging . . . . .	19

2.5.1	fMRI data analysis . . . . .	19
2.6	Arterial spin labelling . . . . .	20
<b>3</b>	<b>Literature review</b>	<b>23</b>
3.1	Gradient echo ( $T_2^*$ ) techniques . . . . .	23
3.1.1	Ischemia-reactive hyperemia . . . . .	24
3.1.2	Cycled hyperoxia . . . . .	25
3.1.3	Muscle contractions . . . . .	25
3.2	Muscle functional magnetic resonance imaging . . . . .	26
3.3	Arterial spin labelling . . . . .	26
3.3.1	Combined BOLD with ASL . . . . .	27
3.4	Fast acquisition techniques . . . . .	27
3.4.1	Echo planar imaging . . . . .	27
3.4.2	Spiral imaging . . . . .	28
<b>4</b>	<b>Problem definition and hypothesis</b>	<b>29</b>
4.1	Problem definition . . . . .	29
4.2	Proposed solution . . . . .	29
4.2.1	Hypothesis . . . . .	30
<b>5</b>	<b>Motion confound to functional imaging of skeletal muscle</b>	<b>31</b>
5.1	Introduction . . . . .	31
5.2	Materials and methods . . . . .	31
5.2.1	Acquisition hardware . . . . .	31
5.2.2	Scanning sessions . . . . .	32
5.2.3	Motion correction . . . . .	32
5.2.4	Analysis . . . . .	32
5.3	Results and Discussion . . . . .	33
5.4	Conclusions . . . . .	34
5.5	Force standardization and motion elimination . . . . .	35
5.5.1	Ergometer . . . . .	36
<b>6</b>	<b>Comparison of echo planar and two shot spiral in-out imaging</b>	<b>39</b>
6.1	Materials and methods . . . . .	39
6.1.1	Acquisition hardware . . . . .	39
6.1.2	Scanning sessions . . . . .	40
6.1.3	Spiral imaging . . . . .	40
6.1.4	Echo planar imaging . . . . .	42
6.1.5	Subjects . . . . .	42
6.2	Results and discussion . . . . .	43
6.2.1	Spiral weighting schemes . . . . .	45

6.2.2	K-space navigation . . . . .	47
6.2.3	Concomitant field effects . . . . .	47
6.3	Conclusions . . . . .	48
<b>7</b>	<b>Arterial spin labelling development</b>	<b>49</b>
7.1	Introduction . . . . .	49
7.2	Materials and methods . . . . .	49
7.2.1	Acquisition hardware . . . . .	49
7.2.2	Pulse sequence . . . . .	49
7.2.3	Brain imaging . . . . .	50
7.2.4	Leg imaging . . . . .	50
7.3	Results and discussion . . . . .	51
7.3.1	Brain imaging . . . . .	51
7.3.2	Leg imaging . . . . .	51
7.4	Conclusions . . . . .	53
<b>8</b>	<b>Conclusions and future work</b>	<b>59</b>
8.1	Arterial spin labelling improvements . . . . .	59
8.1.1	BOLD-ASL interleaved imaging . . . . .	60
8.2	Myoglobin spectroscopy . . . . .	61
8.3	Optical methods . . . . .	61
8.4	Development of protocol and normal data . . . . .	61
8.4.1	New ergometer . . . . .	62
8.5	Goal . . . . .	63
<b>A</b>	<b>Motion correction shell script</b>	<b>65</b>
	<b>Glossary</b>	<b>71</b>
	<b>Bibliography</b>	<b>75</b>

# List of Figures

1.1	Cross-section of lower leg . . . . .	4
2.2	GRE signal . . . . .	12
2.3	Spoiled gradient echo pulse sequence . . . . .	13
2.4	EPI k-space trajectory . . . . .	14
2.5	BOLD EPI pulse sequence . . . . .	15
2.6	Spiral k-space trajectory . . . . .	17
2.7	Spiral BOLD pulse sequence . . . . .	18
2.8	FAIR pulse sequence . . . . .	21
5.9	Isometric exercise . . . . .	33
5.10	Through-plane shift parametric map . . . . .	34
5.11	Twisting motion . . . . .	35
5.12	Elastic ergometer diagram . . . . .	37
5.13	Elastic ergometer photo . . . . .	37
6.14	Multi-shot comparison . . . . .	41
6.15	Spiral in-out pulse sequence . . . . .	42
6.16	Multi-shot EPI artifact . . . . .	43
6.17	EPI and spiral image results . . . . .	44
6.18	EPI and spiral geometry comparison . . . . .	44
6.19	BOLD signal time course . . . . .	45
7.20	Brain ASL images . . . . .	51
7.21	Functional imaging of alternating hand motor task . . . . .	52
7.22	ASL leg images . . . . .	53
7.23	ASL susceptibility artifact from venous outflow . . . . .	55
7.24	Single coil images . . . . .	56
7.25	Fieldmaps from leg and brain . . . . .	56
7.26	Muscle deformation in plantar flexion . . . . .	57
8.27	Pulley Ergometer . . . . .	62
8.28	Lode ergometer . . . . .	63

# List of Tables

1.2	Muscle Contractions . . . . .	2
1.3	ATP synthesis pathways . . . . .	3
6.4	EPI and spiral BOLD signal change . . . . .	46
6.5	Weighting scheme results . . . . .	47

# Symbols and Acronyms

$\alpha$	flip angle; 10
1RM	one repetition maximum; 61
ABI	ankle-brachial index; 6, 29
ACh	acetylcholine; 2
ADP	adenosine diphosphate; 2
ANT	anterior compartment; 43
ASL	arterial spin labelling; 20, 26, 49
ASO	arteriosclerosis obliterans; 4
ATP	adenosine triphosphate; 2
BASH	Bourne-again shell; 65
BOLD	blood oxygenation level dependent; 19, 31, 39
CASL	continuous arterial spin labelling; 20
CBF	cerebral blood flow; 26, 27
CE-MRA	contrast enhanced magnetic resonance angiography; 23
CTA	computed tomography angiography; 6
deoxyHb	deoxyhaemoglobin; 19
DOF	degrees of freedom; 32
DSA	digital subtraction angiography; 6
EMF	electromotive force; 8
EPI	echo planar imaging; 12, 39
FAIR	flow-sensitive alternating inversion recovery; 20, 26, 49
FFT	fast Fourier transform; 15

FG	fast glycolytic; 3
FLASH	fast low-angle shot; 60
fMRI	functional magnetic resonance imaging; 26
FO	fast oxidative; 3
FOV	field of view; 9
FWHM	full width at half maximum; 34
GLM	general linear model; 19, 31
GRE	gradient echo; 19
HOS	higher order shimming; 53
ISMRM	International Society for Magnetic Resonance in Medicine; 27
LAT	lateral compartment; 42
LDF	laser doppler flowmetry; 24
LG	lateral gastrocnemius; 42
mfMRI	muscle functional magnetic resonance imaging; 26
MG	medial gastrocnemius; 42
MRA	magnetic resonance angiography; 6
MRI	magnetic resonance imaging; 1, 7
MVC	maximum voluntary contraction; 57, 61
NIRS	near infrared spectroscopy; 25, 61
NSF	nephrogenic systemic fibrosis; 23
oxyHb	oxyhaemoglobin; 19
PASL	pulsed arterial spin labelling; 20
Pi	inorganic phosphate; 2
PVD	peripheral vascular disease; 4, 29
QUIPSS	quantitative imaging of perfusion using a single subtraction; 60
RF	radio-frequency; 8
RMS	root-mean-squared; 50, 56

ROI	region of interest; 26
SAR	specific absorption rate; 26
SNR	signal-to-noise ratio; 9
SO	slow oxidative; 3
SOL	soleus; 42
SWI	susceptibility weighted imaging; 50
$T_1$	spin-lattice relaxation time constant; 10
$T_2$	spin-spin relaxation time constant; 10
$T_2^*$	measured signal decay time constant; 11
$T_E$	echo time; 11
$T_I$	inversion time; 20
$T_R$	repetition time; 10

# Chapter 1

## Introduction

The work presented in this thesis used two functional magnetic resonance imaging (MRI) methods to image the skeletal muscle of the lower leg. The methods have the potential for the development of a technique to study patients with peripheral vascular diseases. This chapter will include a description of skeletal muscle in general, and the muscles of the lower leg in particular. Following that will be a discussion of peripheral vascular diseases, and the methods commonly used to diagnose them.

### 1.1 Skeletal muscle

#### 1.1.1 Muscle anatomy

Skeletal muscle is a tissue that is attached to bones by tendons. The function of skeletal muscle, as distinct from smooth and cardiac muscle, includes movement, posture, and heat production. Skeletal muscle can contract forcefully in response to a voluntary nerve stimulus. It is also elastic, in that it can be stretched and contract back to its normal length (Seeley et al. 2004).

Skeletal muscles are divided into discrete bundles called fascicles, aligned longitudinally along the tissue, along with blood vessels and nerves. The fascicles are made up of muscle fibres, which are the muscle cells. Muscle cells include multiple nuclei and many mitochondria, as well as highly specialized structures called myofibrils. Myofibrils are the contractile elements of the muscle, and are divided laterally into sections called sarcomeres. Sarcomeres are composed of filaments made of proteins that interact and slide over one another to perform the muscle contraction. Although skeletal muscle cells typically have diameters of 10 to 100  $\mu\text{m}$ , their length can be up to 30 cm (Marieb and Hoehn 2010).

Muscles may be divided into motor units, which are composed of a nerve and all the muscle fibres it supplies. The fibres of a motor unit are not clustered, but are

distributed throughout the muscle.

### 1.1.2 Muscle function

Skeletal muscle can contract in a variety of ways, as shown in **table 1.2** (Marieb and Hoehn 2010). In this study, concentric isotonic contractions occurred, in which the muscle shortens but the tension remains constant.

**Table 1.2:** Muscle Contractions

Contraction Type		Character
Isometric		Constant length
Isotonic	Concentric	Muscle shortens, constant tension
	Eccentric	Muscle lengthens, constant tension

Muscle contraction is initiated when nerve impulses to muscle motor units stimulate the release of calcium ions ( $\text{Ca}^{2+}$ ) into the muscle cells. This occurs through a complex pathway involving acetylcholine (ACh), sodium ( $\text{Na}^+$ ) and potassium ( $\text{K}^+$ ) ions. The  $\text{Ca}^{2+}$  exposes binding sites on the muscle filaments.

If the contraction is to occur, the muscle's energy source, adenosine triphosphate (ATP), must be present. Muscles store enough ATP to sustain only about 4-6 seconds of exercise, so ATP must be re-synthesized constantly from adenosine diphosphate (ADP) and inorganic phosphate (Pi). This occurs in a fraction of a second in one of the three following pathways, which are summarized in **table 1.3**. Direct phosphorylation, an anaerobic energy pathway, occurs when phosphocreatine (PCr, also called creatine phosphate) is consumed in the following reaction:



The other anaerobic pathway is anaerobic glycolysis, in which a glucose molecule is consumed to form 2 ATP. The other products are either pyruvic acid or lactic acid, the latter being produced if  $\text{O}_2$  is in short supply. Finally, aerobic metabolism is the most efficient pathway, producing 32 ATP from one glucose molecule in the mitochondria. The waste products of aerobic metabolism are  $\text{CO}_2$  and  $\text{H}_2\text{O}$ .

Although aerobic respiration can sustain light to moderate intensity exercise for long periods, short duration and very intense exercise requires the anaerobic pathways for energy. The replenishment of the anaerobic pathways requires oxygen, and is partially deferred until it is available. The difference between the amount of oxygen needed to fulfill energy requirements using aerobic metabolism and the amount actually used is called the oxygen deficit (Marieb and Hoehn 2010).

**Table 1.3:** ATP synthesis pathways

	<b>Direct Phosphorylation</b>	<b>Anaerobic Pathway</b>	<b>Aerobic Pathway</b>
Description	equation 1.1	glycolysis	aerobic cellular respiration
Energy	PCr	glycogen, glucose	glycogen, glucose, pyruvic acid, fatty acids
O <sub>2</sub>	none	none	required
Products	1 ATP, creatine	2 ATP, pyruvic acid/lactic acid	32 ATP, CO <sub>2</sub> , H <sub>2</sub> O
Duration	15 seconds	60 seconds	hours

adapted from Marieb and Hoehn (2010)

### 1.1.3 Muscle fibre types

Muscle fibres are categorized according their contraction speed and their predominant energy pathway. The three major types are slow oxidative (SO), fast oxidative (FO), and fast glycolytic (FG). SO fibres are slow to contract, but fatigue resistant, and well suited to endurance exercise. Their primary energy pathway is aerobic metabolism, and they contain large stores of oxygen (bound to myoglobin), and high concentrations of mitochondria. FG fibres contract quickly and forcefully, but fatigue quickly as well. They primarily use the anaerobic glycolysis energy pathway, and have high stores of glucose (as glycogen). FG fibres are typically larger than their SO counterparts. FO fibres are intermediate to the other two, contracting quickly and having both high myoglobin concentrations and large glycogen stores (Marieb and Hoehn 2010).

All muscles contain mixtures of the three fibre types. The proportion of fibre types is somewhat determined genetically, but may also be affected by training. Endurance training may promote FG fibres to convert to FO fibres, increasing the capillary penetration and the amount of myoglobin and mitochondria, which promotes aerobic respiration. Resistance training may have the opposite effect, in which FO convert to FG fibres, causing an increase in glycogen stores, and promoting anaerobic glycolysis.

### 1.1.4 Muscles of the lower leg

The biggest muscles of the lower leg are those in the posterior compartment, which form the bulge of the calf muscle. The calf muscles are the soleus and the two heads of the gastrocnemius (medial and lateral), which are sometimes collectively called the triceps surae (**figure 1.1**). They are involved in plantar flexion of the foot, which is the principle contraction of interest to this project. The muscles of

the lateral compartment (fibularis or peroneus muscles), in addition to performing eversion of the foot, contribute to plantar flexion as well. The muscles of the anterior compartment, principally the anterior tibialis, are important to this study, since they are involved in dorsiflexion of the foot, the opposing motion to plantar flexion (Seeley et al. 2004).

The soleus muscle contracts for long periods to maintain a standing posture, and is composed of a higher proportion of slow oxidative muscle fibres. The gastrocnemius is recruited when high intensity exercise such as running or jumping is performed. The muscle is composed of a greater proportion of fast oxidative and fast glycolytic muscle fibres.

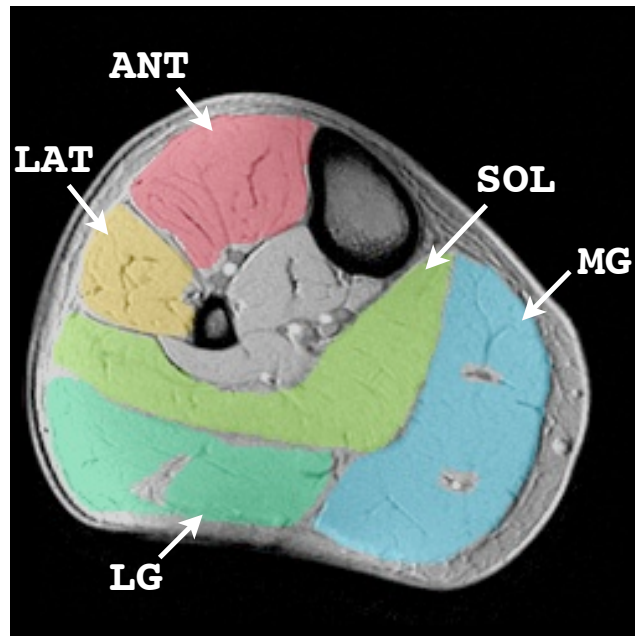


**Figure 1.1: Cross-section of lower leg.** Labelled are the (MG) medial and (LG) lateral heads of the gastrocnemius muscle, (SOL) soleus muscle, (LAT) lateral compartment, and (ANT) anterior compartment.

## 1.2 Peripheral vascular disease

Peripheral vascular disease (PVD) is characterized by reduced perfusion to the limbs. The flow of blood, and hence the delivery of oxygen and nutrients, and removal of wastes and  $\text{CO}_2$ , is impeded in the outer extremities. This is especially true in the arms and lower legs, which can lead to further complications in these areas. The extreme case of PVD is arteriosclerosis obliterans (ASO), in which blood is completely

prevented from flowing through an artery. This means that the blood supply to tissues downstream must come from other arteries, in a process known as collateral circulation, which may not be sufficient (Walker 1980).

PVD occurs primarily in people with atherosclerosis, which is characterized by a build up of plaque on the vessel walls which occludes blood flow. This can be exacerbated by thrombi, which are blood clots on the vessel wall, or emboli. Emboli are blood clots or other particles that travel through the vessels and become lodged in thinner parts of arteries, or where arteries split into two paths.

The primary risk factor for developing PVD is smoking, with 90 percent of affected patients being at least moderate smokers (Marcovitch 2005). Other risk factors for atherosclerosis include hypertension, a high-fat diet, genetic predisposition, age, and diabetes mellitus. The exact mechanism by which diabetes causes atherosclerosis is unproven, but the involvement of protein glycation is a leading hypothesis (Ahmed 2005). This occurs when a reducing sugar reacts with a protein, which may eventually produce practically irreversible structures such as Amadori products and advanced glycation endproducts (AGEs). Protein glycation is more likely with increased severity of hyperglycemia.

As the ischemia worsens in the affected area, the patient will experience increasingly intense intermittent claudication. Intermittent claudication is pain in the lower limbs caused by exercise, which is relieved by rest. If the claudication occurs in the calf muscles, the femoral artery is probably occluded, whereas if the affected area is the foot, either the femoral artery or the anterior or posterior tibial arteries may be blocked (Walker 1980). If the blood flow to the affected area is weak enough, gangrene of the tissue may result. This may be preceded by ulcers and wounds that are slow to heal, especially in the toes and heel. Low nerve response in the feet may compound the problem.

If ASO leads to dry gangrene, in which the tissue withers and turns black, the tissue may be left to slough off on its own. If, however, an infection occurs which leads to moist gangrene, amputation of the ischemic area may be necessary. Lower extremity amputations in people with peripheral vascular diseases is a growing problem (Katsilambros et al. 2003).

### 1.2.1 Testing for PVD

Simple tests for PVD include physical examinations of the lower legs and feet, looking for decreased pulse, low temperature, hair loss, skin changes or ulceration, and a pale colour when the foot is elevated. The blood pooling time in the feet may also be tested, with typical times being about 10 seconds for the filling of the dorsal vein in the foot (Walker 1980).

Intermittent claudication is the most reliable symptom of PVD, and its severity

may be graded based on how far a patient can walk before experiencing pain. This technique for grading PVD may not be reliable, however, as noted by Labs et al. (Labs et al. 1999), and Perakyla et al. (Peräkylä et al. 1998). Lower extremity pain may also be caused by chronic compartment syndrome, nerve root compression, and popliteal cyst (Abul-Khoudoud 2006).

The ankle-brachial index (ABI) may also be computed, which is the ratio of the systolic blood pressure of the posterior tibialis and brachial arteries, respectively, as measured in the supine position with the Doppler modality. Normally the ratio is greater than 1, but may be much lower in people with PVD, with values below 0.5 indicating severe arterial insufficiency, and values below 0.2 suggesting an imminent risk of tissue death (Merli et al. 2004). The post-exercise ABI may be the most reliable indicator of PVD, as noted by Peräkylä et al. (1998). This technique determines only the presence of PVD in the lower limbs, while more sophisticated imaging techniques are required for an indication of the relative severity of the disease along the length of the leg. Disease severity above or below the knee, for example, can have a serious impact on patient quality of life in cases requiring amputation.

Imaging modalities may be used to assess PVD, especially in patients who will receive interventional treatment. Since the usual goal is direct imaging of the arteries to find stenoses, digital subtraction angiography (DSA) is seen as the gold standard imaging technique (Abul-Khoudoud 2006). The procedure has risks associated with ionizing radiation and potentially toxic renal effects of contrast agents. Magnetic resonance angiography (MRA) and computed tomography angiography (CTA) have also been employed to study patients with PVD (Muir 2009). Duplex ultrasound for arterial imaging is also a promising technique (Eiberg et al. 2002).

Doppler ultrasound may be used to measure blood flow velocity in any of the larger arteries including the femoral, popliteal, posterior tibialis and dorsalis pedis arteries. The flow velocity,  $v$ , is calculated as follows,

$$v = \frac{c \cdot \Delta f}{2f \cos \theta}, \quad (1.2)$$

where  $f$  is the initial frequency of the emitted sound wave,  $\Delta f$  is the change in frequency after reflection,  $c$  is the speed of sound in tissue, and  $\theta$  is the angle of the flow with respect to the ultrasound beam. A waveform, indicating the temporal evolution of the blood velocity, may be evaluated for each vessel to determine the health of the blood flow.

The focus of this thesis was the development of optimal MR imaging methods for assessing PVD. Optimization involves development of an appropriate muscle challenge and assessment of an ideal MRI pulse sequence. The remaining introductory chapters will include a discussion of MR physics and a review of earlier publications as related to this problem.

## Chapter 2

# Magnetic resonance imaging

MRI is a modern technique in which subjects are placed in a large, homogeneous magnetic field,  $B_0$ . The magnet can be cryogenic, permanent, or electromagnetic, with a cylindrical or two pole (up-down) geometry. The MRI signal is digitized, and images are reconstructed on powerful computers using 2D and 3D fast Fourier transforms. MRI is tomographic in nature, in that the images are usually viewed as slices through a plane of the body, but various techniques may be viewed as maximum or minimum intensity projections, or as segmented or rendered images.

### 2.1 Signal generation

The signal for MRI comes from protons, chiefly the  $^1\text{H}$  atoms of water ( $\text{H}_2\text{O}$ ) and fat ( $-\text{CH}_2-$  protons). Although the full analysis of physics on such small scales uses quantum mechanics, a general understanding of MRI can be obtained from a classical description, which is much more intuitive. The individual protons (also called spins in this context) have their own magnetic moment. In the absence of a strong external magnetic field, the spins will be randomly oriented, and a volume of tissue will not have a net magnetization. Upon placement of the subject into a magnetic field, some spins will tend to orient in the direction of the field, and the tissue will have a small net magnetization. The spins precess at a frequency proportional to the magnetic field magnitude. This relationship is known as the Larmor equation:

$$\omega = \gamma B \quad , \quad (2.3)$$

where  $\gamma$  is the gyromagnetic ratio for protons,  $2.67 \times 10^8 \text{ rad}/(\text{s}\cdot\text{T})$ .

### 2.1.1 Spatial localization

Given that the spins precess at a frequency proportional to the applied field as in equation 2.3, known spatial deviations in the applied field can be made, which will cause the spins in a particular region to precess at a unique frequency. The tuned radio-frequency (RF) antennas that transmit and receive the signals in MRI are commonly called coils. The components that produce the spatial deviations in the magnetic field are the gradient coils, which typically produce three orthogonal linear magnetic field gradients superimposed on the magnetic field.

Typically the direction along the bore of the magnet is labelled the z-axis, such that an axial view of the subject is in the x-y (transverse) plane. In order to generate a signal, the spins must be tipped into that plane by a specialized RF pulse. For an axial acquisition, a linear gradient would be applied in the z-direction, giving the spins a linear frequency dependence on position:

$$\omega(z) = \gamma G_z z \quad , \quad (2.4)$$

where  $G_z$  is a linear gradient  $dB/dz$ . The spins in the centre of the volume of interest would be precessing at the centre frequency of the transmitted RF, and those in the rest of the slice would be within a range defined by the RF transmit bandwidth. Therefore the slice is selected by a combination of the gradient, RF transmit centre frequency, and RF transmit bandwidth.

Following the RF pulse (in a sequence that uses a single pulse) the spins are precessing in the transverse plane, and they produce a changing magnetic flux that induces an electromotive force (EMF) in a nearby receiver coil. The EMF in the coil,  $\xi$ , is induced according to Faraday's Law:

$$\xi = - \frac{d\phi_B}{dt} \quad , \quad (2.5)$$

where  $\phi_B$  is the magnetic flux through the coil. A current will then be induced in the coil which depends on the EMF, as well as the resistance, capacitance, and inductance of the coil.

In conventional imaging, spatial information within the slice is encoded with linear gradients applied in x- and y-axis. One axis is encoded incrementally using a gradient lobe, applied for a time  $T$ , that produces a spatially dependent phase change,  $\phi$ :

$$\phi(y) = \gamma y \int_0^T G_y dt \quad , \quad (2.6)$$

where  $G_y$  is a linear gradient  $dB/dy$  (Bernstein et al. 2004). The other axis is encoded using a bipolar gradient lobe during signal digitization.

An image can then be obtained from the signal by using the Fourier transform. The Fourier transform is a mathematical tool that can convert a signal into its individual frequency components. Specifically, the discrete Fourier transform is a method of approximating a signal from a finite number of sinusoidal waveforms. The obtained signal can be Fourier transformed to a number of discrete periodic waveforms with frequencies corresponding to their spatial location.

### 2.1.2 K-space

Although the spatial localization phenomenon can be conceptualized entirely by the phase changes produced by the gradients, it is useful to make an analogy to a space navigated by the gradient waveforms, known as k-space (Ljunggren 1983). K-space is the grid onto which the raw MRI data is read. The raw data is the spatial frequency information that is Fourier transformed into image data. The outer area of the k-space grid represents the high frequency image information, or fine features of the image, whereas the centre of k-space determines the overall signal level and the image contrast. The coverage of k-space determines the image field of view (FOV). The signal-to-noise ratio (SNR) and scan time are determined by the contents of k-space.

The extents of k-space in the horizontal and vertical directions are typically labelled  $k_x$  and  $k_y$ , representing frequency encoding and phase encoding, respectively. Similarly, the distances between samples in the two directions are  $\Delta k_x$  and  $\Delta k_y$ . In general, the trajectory in k-space,  $\mathbf{k}$ , is proportional to the time integral of the gradient waveforms,  $\mathbf{g}$  (Bernstein et al. 2004):

$$\mathbf{k}(t) = \frac{\gamma}{2\pi} \int_0^t \mathbf{g}(\tau) d\tau \quad (2.7)$$

Then the step size between k-space points in the frequency encode direction ( $x$ ) is

$$\Delta k_x = \frac{\gamma}{2\pi} g_x(t) \Delta t \quad , \quad (2.8)$$

where  $\Delta t$  is the time between successive samples during frequency encoding. The quantity  $\Delta k_x / \Delta t$  can be regarded as the speed with which the acquisition is travelling through k-space, and it is proportional to the instantaneous gradient magnitude.

The field of view in the frequency encode direction of the resultant image is related to the k-space sampling resolution through the Fourier transform, by:

$$FOV_x = \frac{1}{\Delta k_x} \quad (2.9)$$

Then the resolution in the frequency encode direction,  $\Delta x$ , is related to  $\Delta k_x$  as follows:

$$\Delta x = \frac{1}{N \cdot \Delta k_x} \quad , \quad (2.10)$$

where  $N$  is the number of samples in the frequency encode direction (McRobbie et al. 2006). So high temporal frequency acquisitions are needed to acquire a small field of view for a given matrix size, and broad k-space sampling is needed for high resolution images.

## 2.2 Signal recovery and imaging parameters

The MRI signal is dependant on having spins with magnetization components in the transverse plane, and in phase with one another. The RF pulse applied to the spins may be designed to tip the spins entirely into the transverse plane, in which case it is said to have a flip angle ( $\alpha$ ) of  $90^\circ$ . A gradient echo sequence has a single RF pulse and uses a gradient for spin magnetization refocusing. The RF pulse can have any flip angle, but  $\alpha$  is typically less than  $90^\circ$ , which produces less magnetization in the transverse plane, and a decreased signal. For example, a flip angle of  $30^\circ$  would produce a signal  $\sin(30^\circ) = 1/2$  as large as a  $90^\circ$  one, at least on the first repetition.

Immediately after the spins have been flipped into the transverse plane, they start to recover back along the z-axis. The recovery of the magnetization follows an exponential curve, and the time constant of the recovery is called  $T_1$ .  $T_1$  is a characteristic property of the tissue being evaluated, and depends on the field strength. The  $T_1$  of skeletal muscle at 3.0 T has been measured in the abdomen as  $900 \pm 30$  ms (de Bazelaire et al. 2004), in the leg as  $1420 \pm 40$  ms (Gold et al. 2004), and in mice as  $1410 \pm 10$  ms (Stanisz et al. 2005). This value affects the image contrast through the repetition time ( $T_R$ ), the time from one application of an RF pulse until the next application when the next increment of k-space is collected. If the repetition time is not long enough to allow full relaxation of the spins along the z-axis, the result is some  $T_1$ -weighting of the image contrast. The shorter the  $T_R$ , the greater the  $T_1$ -weighting. This can be mitigated to some extent by the use of smaller flip angles; smaller flip angles take less time to fully recover, meaning that they produce less  $T_1$ -weighting.

While there is still some transverse magnetization, the individual spins in a voxel of tissue will weakly interact with one another and lose coherence in their phase. When the spins are no longer in phase, no signal can be acquired from the voxel. After the initial RF pulse puts the spins in phase, they begin to de-phase exponentially with a time constant  $T_2$ .  $T_2$  is a property of tissues independent of  $T_1$ . The short  $T_2$  of skeletal muscle at 3.0 T has been measured in the abdomen as  $29 \pm 4$  ms (de Bazelaire

et al. 2004), in the leg as  $32 \pm 2$  ms (Gold et al. 2004), and in mice as  $50 \pm 4$  ms (Stanisz et al. 2005). The  $T_2$  of human blood has been measured as  $275 \pm 50$  ms (Stanisz et al. 2005).  $T_2$  and the choice of echo time ( $T_E$ ) affect the image contrast; if the  $T_E$  is similar to  $T_2$ , the image will be  $T_2$ -weighted.  $T_2$ -weighted images are acquired with spin-echo pulse sequences.

Another parameter,  $T_2^*$ , is closely related to  $T_2$ . While  $T_2$  is the decay constant associated with spin-spin interactions,  $T_2^*$  is the decay constant that incorporates dephasing due to intrinsic tissue effects and the non-homogeneity of the local magnetic field (Hashemi and W. G. Bradley 1997), as follows:

$$\frac{1}{T_2^*} = \frac{1}{T_2} + \frac{1}{T_2'} \quad (2.11)$$

The factor  $1/T_2'$  is often equated to  $\gamma\Delta B_0$ , an expression of the local inhomogeneity in the main magnetic field. Because of the influence of magnetic field homogeneity,  $T_2^*$  is dependent upon field strength.  $T_2^*$ -weighted images are acquired with long echo times using gradient echo pulse sequences or asymmetric spin echo sequences.

## 2.3 Gradient echo pulse sequence

The gradient echo pulse sequence is characterized by a negative gradient lobe immediately preceding the read gradient, which de-phases the spins, as shown in **figure 2.3**. The negative lobe has an area half as large as the read gradient, such that the spins are in phase at the centre of the read gradient. The signal,  $s$ , obtained from a gradient echo pulse sequence is given as follows:

$$s = \rho \cdot \frac{\sin \alpha \cdot \left[ 1 - \exp\left(\frac{-T_R}{T_1}\right) \right] \cdot \exp\left(\frac{-T_E}{T_2^*}\right)}{1 - \cos \alpha \cdot \exp\left(\frac{-T_R}{T_1}\right)}, \quad (2.12)$$

where  $\rho$  is a proportionality constant including the proton density (McRobbie et al. 2006). A plot of the equation is shown in **figure 2.2**.

If a high flip angle (close to  $90^\circ$ ) is used, the spins have very little magnetization in the  $M_z$  direction when the subsequent RF pulse arrives. The result is very low signal. An optimum flip angle, called the Ernst angle, can be calculated to maximize the signal for a spoiled GRE scan for a particular  $T_R$ . The Ernst angle may be obtained by setting the derivative of the signal equation to zero, obtaining,

$$\alpha_{Ernst} = \cos^{-1} \left[ \exp\left(\frac{-T_R}{T_1}\right) \right], \quad (2.13)$$

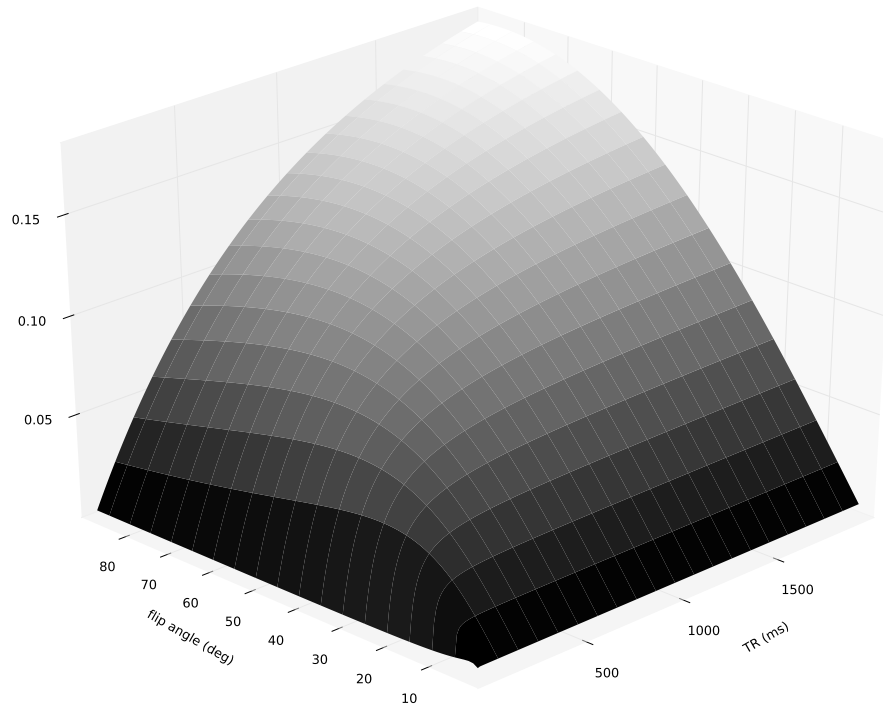


**Figure 2.2: GRE signal.** The plot of equation 2.12 shows the expected signal given a range of  $T_R$  and  $\alpha$  values. The plot was made with  $\rho = 1$ ,  $T_E = 40$  ms,  $T_1 = 900$  ms, and  $T_2^* = 25$  ms.

A gradient echo pulse sequence with a 40 ms  $T_E$  is shown in **figure 2.3**. The spoiler gradient is used to eliminate any residual transverse magnetization by dephasing the spins, after the data from a particular echo is acquired. This pulse sequence acquires one line of k-space per echo, as is conventional. This results in image acquisition times on the order of minutes.

## 2.4 Fast acquisition techniques

Typically, functional imaging techniques require rapid acquisition strategies to see changes with time. To obtain the highest temporal resolution, all the data for one image should be obtained from a single echo (or shot). There are several methods to accomplish this, with the most common being echo planar imaging (EPI). Spiral imaging is another popular method of filling k-space for functional imaging.

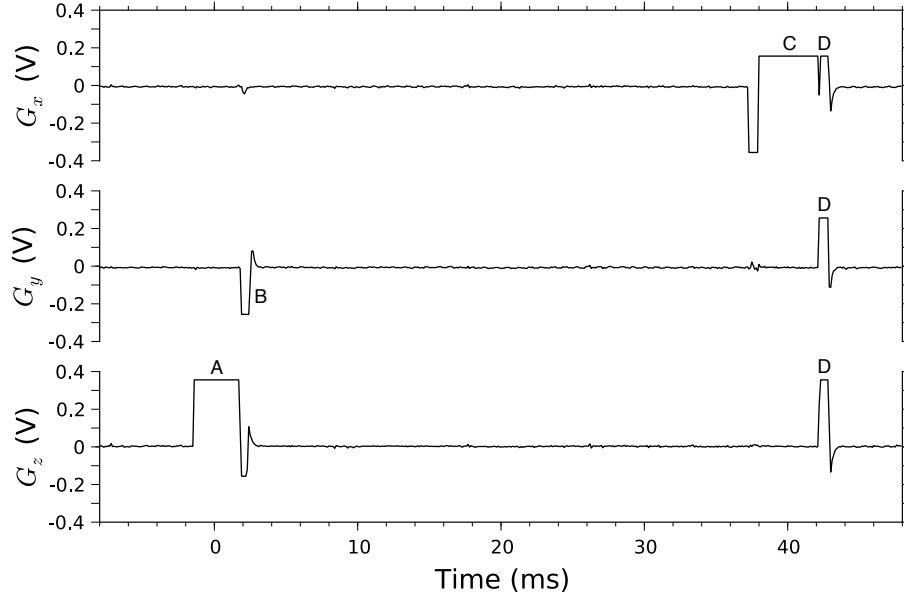


**Figure 2.3: Spoiled gradient echo pulse sequence.** **(A):** Slice select gradient – the RF pulse at flip angle  $\alpha$  is applied during this time. The negative gradient lobe compensates for the de-phasing effect of the slice select gradient. **(B):** Phase encode gradient – navigates to a new k-space line,  $k_y$ . **(C):** Read gradient – traverses k-space along  $k_x$ . The RF data is acquired during this time. The initial negative lobe de-phases the spins so that the echo is created at 40 ms. **(D):** Spoiler gradients – de-phase any remaining  $T_2$  magnetization.

### 2.4.1 Echo planar imaging

A common sequence follows cartesian path through k-space, as in **figure 2.4**. The pulse sequence that produces the path is shown in **figure 2.5**. The  $G_x$  gradient causes the spins to de-phase in opposite directions with alternating applications of the gradient lobes, while the  $G_y$  gradient blips increase the phase in the y-direction by increments of a single line.

The main artifacts associated with the EPI acquisition are geometric distortion (stretching) in the phase encode direction, and ghosting due to phase errors (Jezzard and Balaban 1995). The geometric distortion occurs during the acquisition because off-resonant spins acquire phase which is unrelated to the gradients. The artifact is usually most prominent near areas prone to off-resonance effects, such as near the sinuses and ear canals lateral to the brain. Because the leg has such broad tissue-bone interfaces, off-resonance artifacts can be very troubling. Furthermore, because

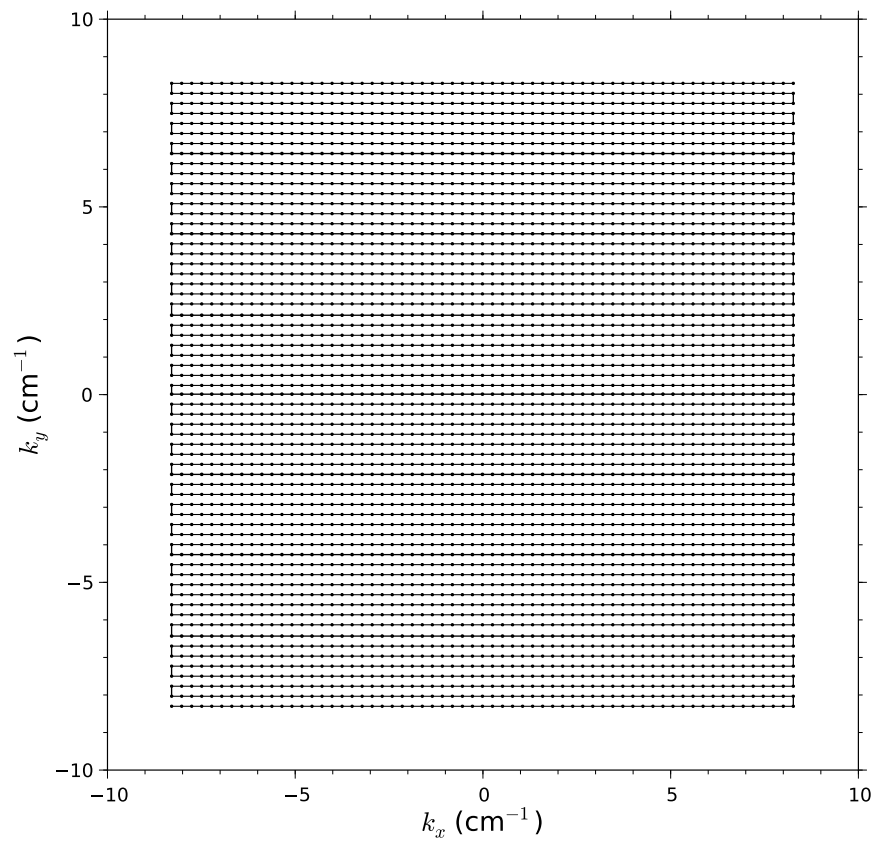


**Figure 2.4: EPI k-space trajectory.** The trajectory follows a Cartesian path along the frequency encode lines from one edge of the phase-encode direction to the other.

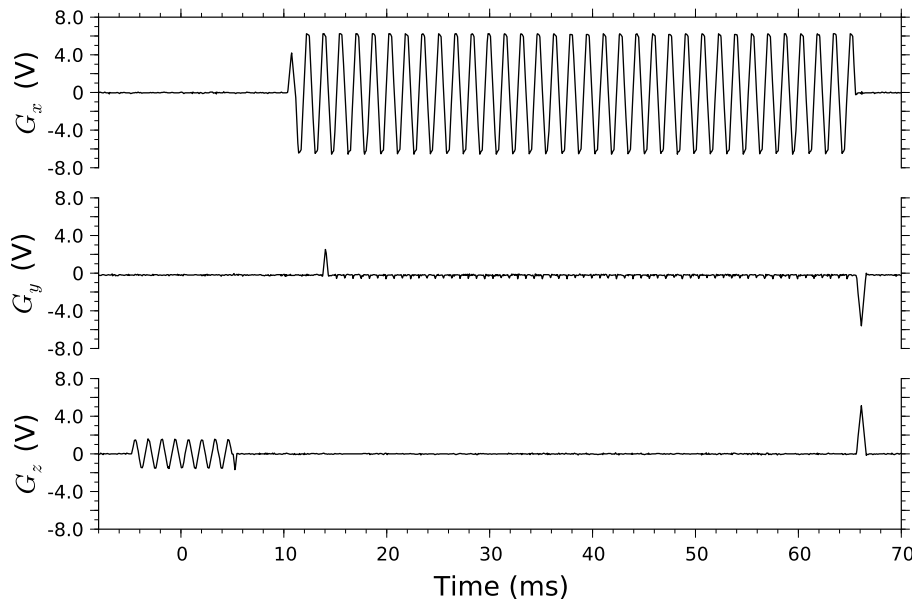


**Figure 2.5: BOLD EPI pulse sequence.** The pulse sequence shows how EPI k-space filling is accomplished with the gradients. Note that the  $G_z$  waveform indicates a spectral spatial applied to reduce the fat signal. Also note that the  $G_x$  waveforms are not square, which was compensated in the scanner’s acquisition using the ramp sampling feature.

shimming is more difficult in long cylindrical objects, compared to spheres (e.g. the head), EPI scans are more challenging in the legs.

The other problem associated with EPI occurs when attempting to perform multi-shot acquisitions. Although EPI data acquired across multiple echoes has the potential to increase resolution and reduce off-resonance artifacts, the technique is highly sensitive to bulk motion, producing ghost-like out-of-phase artifacts (Robson et al. 1997). This is discussed in further detail in section 6.1.4.

### 2.4.2 Spiral imaging

The spiral acquisition typically begins at the centre of k-space and winds in a continuous curve around the central point, as shown in **figure 2.6**. **Figure 2.7** shows the spiral pulse sequence that produces the k-space trajectory. The spiral acquisition is non-cartesian, meaning that re-gridding to a cartesian co-ordinate system is necessary before the fast Fourier transform (FFT) can be performed. The re-gridding procedure is not typically problematic, although oversampling has been recommended (Block and Frahm 2005).

A  $B_0$  field-map is acquired during spiral imaging, typically using the first two image acquisitions of the sequence. The field-map is calculated from two phase images acquired with slightly differing  $T_E$ , as follows (Haacke et al. 1999):

$$\Delta B(\mathbf{r}) = \frac{\phi(\mathbf{r}, T_{E_2}) - \phi(\mathbf{r}, T_{E_1})}{\gamma \cdot (T_{E_1} - T_{E_2})} \quad (2.14)$$

The expression can be expressed in terms of offset frequency,  $\Delta f$ , by multiplying with  $\gamma/(2\pi)$ . Linear correction is the simplest method of using the field-map to reduce blurring in a spiral image (Irrazabal et al. 1996). In this method, the offset frequencies are fit to a spatially varying function:

$$\Delta f = f_0 + f_x x + f_y y \quad (2.15)$$

Each scan plane is assigned a constant frequency offset,  $f_0$ , and the two parameters  $f_x$  and  $f_y$  (Bernstein et al. 2004). The resulting phase shifts can be calculated from the offset frequencies, as  $\Delta\phi = 2\pi\Delta f t$ , where  $t$  is the time since RF excitation. The in-plane k-space shifts can then be calculated from  $\Delta k_x(t) = f_x t$ , and  $\Delta k_y(t) = f_y t$ . These k-space offsets are used to more faithfully represent the k-space trajectory before re-gridding occurs.

Spiral imaging is said to have less stringent requirements on the gradient hardware compared to EPI, since square gradient shapes are not necessary (Takahashi et al. 1997). The slew rate limited spiral equation derived by Glover is as follows (Glover and Law 2001):

$$\mathbf{k}(t) = \alpha t^{2/3} [\cos(\beta t^{2/3})\mathbf{a}_x + i \sin(\beta t^{2/3})\mathbf{a}_y] \quad , \quad (2.16)$$

where

$$\alpha = \frac{\pi}{p T_{acq}^{2/3}} \quad , \quad \beta = D\alpha \quad , \quad p \equiv \frac{D}{N} \quad , \quad (2.17)$$

where  $p$  is the pixel size,  $D$  is the field-of-view,  $N$  is the image matrix size, and  $T_{acq}$  is the acquisition time. The scanner's slew rate is the maximum rate at which it can change the gradient amplitude. The image acquisition time resulting from a 100kHz BW, 64x64 image, with a 24 cm FOV is  $T_{acq} = 17.384$  ms (Li et al. 2006). **Figure 2.6** shows the resulting k-space trajectory, with the pulse sequence that produces the trajectory in **figure 2.7**.

Spiral imaging samples the centre of k-space to a greater degree than the exterior, as shown in **figure 2.6**. Because the centre of k-space is the source of most of the image signal, spiral imaging has been found to offer higher temporal stability and sensitivity in functional brain imaging (Yang et al. 1998). Spiral imaging has also been shown to offer greater resolution given the same acquisition window (Klarhöfer

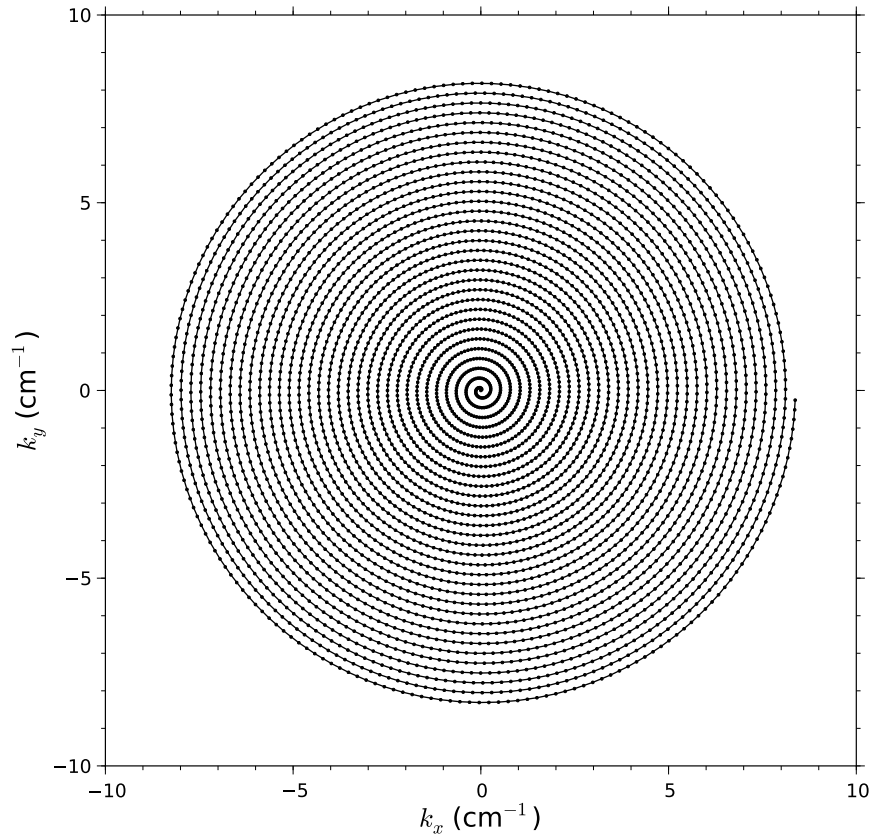


**Figure 2.6: Spiral k-space trajectory.** In this spiral-out path, the trajectory starts from the centre and spirals outward around the central point. The parametric plot was produced from equation 2.16. Note that the sequence is optimized for slew rate limitations, and does not have a constant angular velocity. The sampling time and the acquisition time are  $\Delta t = 4 \mu\text{s}$  and  $T_{acq} = 17.384 \text{ ms}$ .

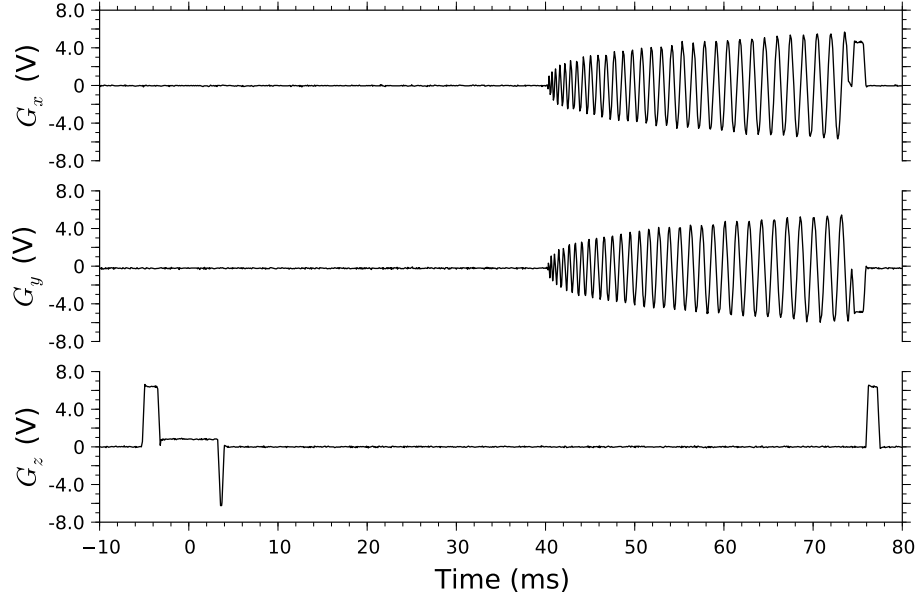


**Figure 2.7: Spiral BOLD pulse sequence.** The pulse sequence produces the spiral k-space trajectory. Note that the centre of k-space is sampled at 40 ms, which generates the BOLD contrast for the image.

et al. 2002), due to its more efficient use of the gradients. Furthermore, Nishimura et al. used simulations to assert that spiral imaging is less sensitive to pulsatile flow in a vessel within the imaging plane (Nishimura et al. 1995). Based on the simulation, the authors predicted that EPI would produce distortion and ghosting artifacts, whereas the flow had little effect on spiral.

Spiral imaging is a flexible technique, in that multiple acquisitions can be made from a single echo without a significant  $T_R$  penalty. This is accomplished by acquiring one spiral before the echo and one after. Although EPI remains the most widely available and widely used technique, spiral imaging is worth examining for its potential benefits.

The main artifact associated with spiral imaging is ring-shaped blurring due to off-resonant spins (Block and Frahm 2005). As in EPI, the off-resonant artifacts in the spiral acquisition increase with the duration of the readout time,  $T_{acq}$  (Bernstein et al. 2004). The amount of blurring should be reduced for an interleaved sequence, since  $T_{acq}$  is reduced as the number of interleaves is increased.

## 2.5 Blood oxygenation level dependant imaging

Blood oxygenation level dependent (BOLD) imaging produces a signal that depends on the ratio of oxyhaemoglobin (oxyHb) to deoxyhaemoglobin (deoxyHb) in the blood. The signal intensity is affected because oxyHb is diamagnetic, whereas deoxyHb is paramagnetic. When large amounts of deoxyHb are present in the blood, the local change in magnetic susceptibility causes a decrease in  $T_2^*$  in the vicinity of the vessel (Buxton 2002). Since  $T_2^*$  is longer for blood that has higher  $O_2$  saturation, more deoxygenated blood appears darker than surrounding tissue. Since the magnetic field is affected for some distance from the blood vessel, the tissue surrounding the vessel may have decreased signal as well.

In order to detect the difference, a pulse sequence sensitive to  $T_2^*$  effects must be used, such as a gradient echo (GRE) sequence with a long  $T_E$ . Multi-echo GRE sequences are sometimes used as well, giving the ability to fit an exponential curve to the signal intensity from multiple time-points and calculate a  $T_2^*$ -map.

### 2.5.1 fMRI data analysis

Two methods are common for analyzing functional MRI data from brain imaging: general linear model (GLM) and correlation analyses. The general linear model involves a linear fit of each voxel's signal time series,  $y(t)$  to a linear model,  $x(t)$ . This can be expressed as

$$y(t) = a \cdot x(t) + b + e(t) \quad , \quad (2.18)$$

where  $a$  and  $b$  are the parameters to be estimated in the fit, and  $e(t)$  is a residual, or error term (Boslaugh and Watters 2008). A least squares fit is performed to minimize the value of  $\sum_{i=1}^n (y_i - a \cdot x_i + b)$ , often using a square wave based model for  $x(t)$ . A  $t$ -statistic may then be calculated from the quotient of  $a$  and the standard deviation of the error term, which can be converted to a  $p$ -value.

The correlation analysis method involves the calculation of Pearson's product-moment correlation coefficient,  $r$  (Boslaugh and Watters 2008):

$$r = \frac{1}{n-1} \sum_{i=1}^n \left( \frac{x_i - \bar{x}}{s_x} \right) \left( \frac{y_i - \bar{y}}{s_y} \right) \quad , \quad (2.19)$$

where  $x$  and  $y$  are the model and measured values, respectively. The correlation method is useful because it takes into account anti-correlative behaviour automatically, ranging from -1 to 1.

Typically the statistical correlation values are calculated for each voxel, and then the map is thresholded to a particular  $p$ -value or  $z$ -score. Cluster filtering is also commonly applied to eliminate the spurious results that inevitably occur with the

large number of sample points in a BOLD data set. Clustering is typically a nearest-neighbour threshold, such that each correlated voxel must have a minimum number of neighbouring correlated voxels, or it is eliminated.

## 2.6 Arterial spin labelling

Arterial spin labelling (ASL) is an imaging technique for measuring microvascular blood perfusion. The ASL signal can be quantified, yielding values with units of ml/(100g of tissue·min). ASL involves the use of a saturation or inversion pulse to give some blood an endogenous label. When the labelled blood flows into another area of tissue, it can be detected in the image (Vlaardingerbroek and den Boer 2003). There are two main types of ASL pulse sequences. The first is continuous arterial spin labelling (CASL), in which a steady supply of labelled blood flows into the imaging plane. The other type is pulsed arterial spin labelling (PASL), in which there is a short delay between the labelling pulse and the image acquisition, to give the labelled blood time to flow.

A common PASL technique is known as flow-sensitive alternating inversion recovery (FAIR). First, a non-selective  $180^\circ$  inversion pulse is applied to the entire tissue within the coil, without the use of a slice-select gradient (Buxton 2002). After the so-called inversion time ( $T_I$ ) has passed, a spin echo or gradient echo imaging sequence is initiated, using parameters to acquire a  $T_1$ -weighted image. By subtracting an image that applied the inversion pulse selectively to the imaging plane only, the signal from the in-flowing blood can be isolated, as the perfusion is proportional to the difference in magnetization,  $\Delta M$  (Bernstein et al. 2004). The two components of the FAIR pulse sequence shown in **figure 2.8**.

The FAIR technique has several advantages over earlier ASL pulse sequences, allowing multi-slice acquisition, and removing the need to know the directionality of in-flowing blood. One limitation of the FAIR sequence is sensitivity to arterial transit time, especially in multi-slice acquisitions (Wong et al. 1998). Arterial transit time is the time taken for blood to travel from the labelling plane to the image slice. As a result, many regard perfusion maps generated from the FAIR sequence to be merely qualitative, rather than truly quantitative measures of perfusion.

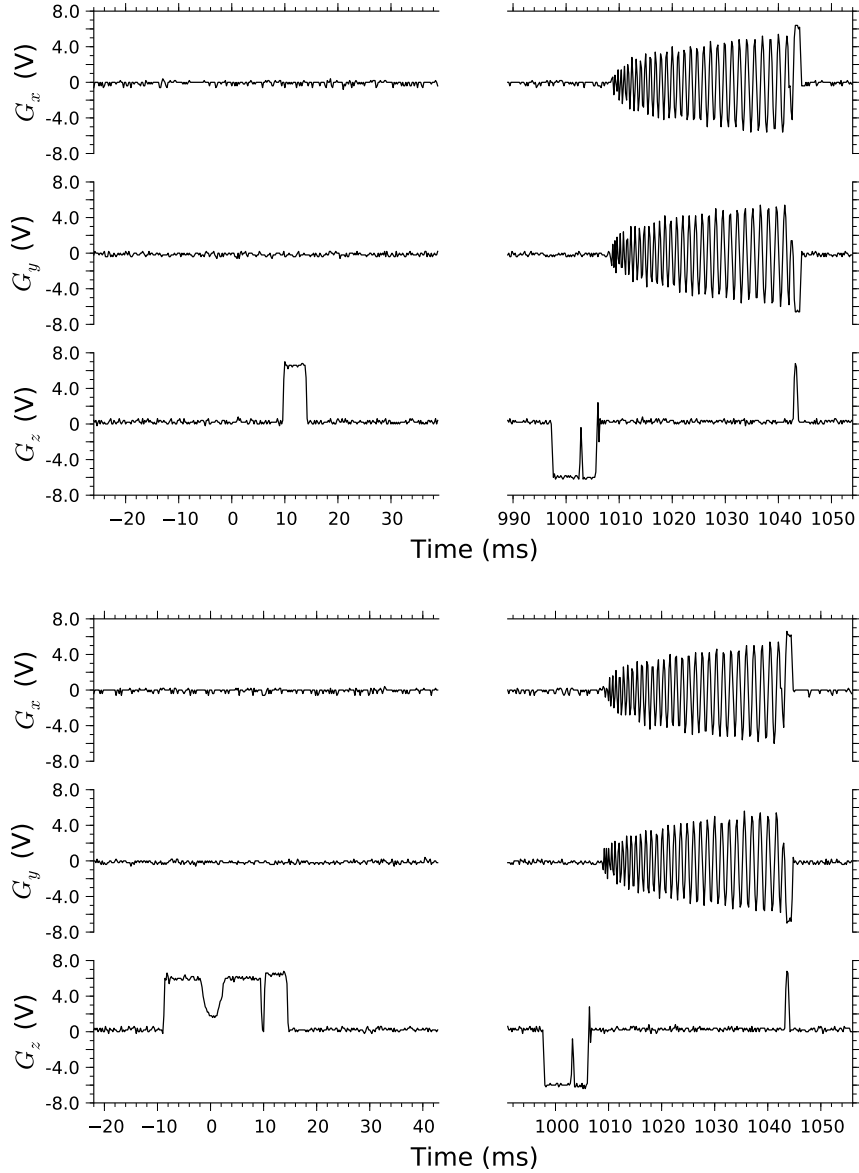


**Figure 2.8: FAIR pulse sequence.** The two components of the FAIR ASL sequence are shown. Note that the  $T_I$  of the sequence is 1200 ms. **(Top):** in the absence of a slice select gradient during the inversion pulse (time=0), all spins within the coil are inverted. This is the labelling, or tagging, sequence. **(Bottom):** The slice select gradient is present, and only the spins in the imaging slice are inverted. This is the unlabelled, or control, sequence. Subtracting the labelled image from the control image gives an image proportional to perfusion.



# Chapter 3

## Literature review

The traditional MRI method for imaging the vasculature of the lower legs is contrast enhanced magnetic resonance angiography (CE-MRA). This technique involves the intravenous injection of a contrast agent containing gadolinium. Gadolinium injection is contraindicated in some patients with PVD, since they may have reduced circulation to their kidneys, and thus reduced function. With reduced kidney function, the injection of gadolinium containing contrast agents causes an increased risk of developing nephrogenic systemic fibrosis (NSF), a potentially fatal disease.

This chapter will review previous research that has contributed knowledge to the present study. The focus will be on functional MRI imaging techniques that do not require contrast.

### 3.1 Gradient echo ( $T_2^*$ ) techniques

The BOLD effect was first described by Ogawa et al. (1990). Their images were acquired at very high field strengths, and involved the direct imaging of blood vessels in rat brains due to the presence of paramagnetic deoxyhemoglobin. Used in lower field strength (1.0-3.0 T) studies on humans, the BOLD effect became important in functional imaging of the brain.

A naive approach would be to record BOLD data or  $T_2^*$  maps, without normalization to a standard, and compare signal levels or  $T_2^*$  values across subjects. This method is problematic because  $T_2^*$  depends on the geometry of the object being scanned, as well as the scanner itself. A better method is to perturb the blood oxygenation of the muscle in some way and analyze the change in signal. A common approach in muscle is ischemia. This method involves occlusion of the blood supply using an inflated pressure cuff for a pre-determined time, typically several minutes. BOLD data is acquired continuously during the occlusion and after the blood supply

is restored, during reactive hyperemia. Other methods of changing blood oxygenation include hyperoxia, hypercapnia, various vasodilators and vasoconstrictors (Bulte et al. 2004, 2006), and exercise.

### 3.1.1 Ischemia-reactive hyperemia

Lebon et al. were, to the best of my knowledge, the first to apply the BOLD technique to human skeletal muscle (Lebon et al. 1998a,b). In Lebon et al. (1998b), the group used a multi-echo GRE sequence to calculate the  $T_2^*$ -map, and used the extrapolated signal intensity at  $T_E=0$  as a measure of perfusion. They used an ischemia-reactive hyperemia protocol to perturb the muscle oxygenation, with the results showing the decrease in  $T_2^*$  during ischemia and large overshoot during hyperemia, as well as a peak in the perfusion data upon cuff removal. In Lebon et al. (1998a), the group provided evidence for the existence of the muscle BOLD effect. They used a GRE sequence to acquire  $T_2^*$ -weighted images, and interleaved a spectroscopic sequence to obtain information about the deoxygenation of myoglobin. Again using ischemia-reactive hyperemia, they plotted the time evolution of the  $T_2^*$  signal (averaged over an ROI within each muscle group) and the simultaneously acquired myoglobin desaturation signal. The two signals were complementary.

A 2006 study by Duteil et al. used ASL and BOLD techniques to study the calf muscle under post-ischemic reactive hyperemia. The study found that perfusion strongly influenced the BOLD signal response. The authors emphasized the importance of using ASL as well as BOLD to elicit the underlying cause of BOLD signal changes.

Ledermann et al. (2006b) used BOLD during post-ischemic reactive hyperemia to study the calf muscles of patients with PVD. The study found that the signal intensity change was smaller in patients with PVD compared to healthy controls, and the time-to-peak of the signal change was delayed in those with PVD.

Another study by Ledermann et al. (2006a) compared the BOLD signal intensity with laser doppler flowmetry (LDF) and transcutaneous oxygen pressure (TcPO<sub>2</sub>) measurements. The study imaged the calf muscles using an ischemia-reactive hyperemia paradigm. They concluded that the BOLD signal intensity profile has “moderate to good” agreement with LDF and TcPO<sub>2</sub>, two techniques more established for assessing patients with PVD.

Recently Schulte et al. (2008) used an ischemia-reactive hyperemia paradigm to examine the effects of aging on the BOLD signal. They studied the BOLD signal time course in healthy young adult and elderly volunteers. The study found significant differences in the time course of the signal, notably a decrease in the percent change of the peak signal intensity in the older group.

### 3.1.2 Cycled hyperoxia

In 2003, Noseworthy et al. applied BOLD imaging to human calf muscles using a novel paradigm. The signal change corresponding to the alternate breathing of 100% oxygen and normal air was observed. The signal in some voxels was found to correlate with a square wave model that included a suitable delay time. After exercise, the number of correlated voxels was found to increase. Bulte et al. (2006) studied the BOLD signal using the same hyperoxia cycling paradigm as in Noseworthy 2003. Pre- and post-exercise scans were performed, and the number of correlated voxels was found to depend strongly on the vasomodulators caffeine and antihistamine.

### 3.1.3 Muscle contractions

Exercise is perhaps the most natural method of perturbing muscle perfusion and oxygenation, and is physiologically relevant to sufferers of claudication. Several BOLD studies have used exercise, either as brief, single contractions, or sustained isometric contractions.

In a 2004 paper, Meyer et al. studied the BOLD signal intensity after single contractions of the upper and lower legs, as well as the forearms. A 40-45 ms  $T_E$  was used, and several parameters were varied, including  $T_R$  (500/2000 ms), pulse sequence, field strength, and contraction force. The transient increase in signal intensity following the contractions was not found to vary with the  $T_R$  or pulse sequence (GRE/SE), but  $\Delta SI$  increased significantly with both force and field strength. The group also generated correlation maps using an arbitrary idealized waveform. Correlation to the model was found to be strong in the recruited muscles.

Wigmore et al. (2004) used a short  $T_E$  ( $T_R/T_E/\alpha=500$  ms/18.6 ms/90°) gradient echo sequence to acquire data following single contractions at various intensities. The group compared the signal change with venous occlusion plethysmography and found good correlation between the two signals, indicating that the signal at this  $T_E$  is perfusion-weighted.

In 2005, Towse et al. studied the transient BOLD signal ( $T_R/T_E/\alpha=1000$  ms/40 ms/90°) increase after brief contractions in sedentary and active individuals. The signal increase was found to be much greater, and persisted longer, in the active group.

More recently, Damon et al. (2007a) sought to further elucidate the source of the BOLD signal ( $T_R/\alpha=1000$  ms/90°) after brief muscle contractions. They used two GRE pulse sequences with echo times of 6 and 46 ms, and compared the data with near infrared spectroscopy (NIRS) measures of blood volume and oxyhemoglobin saturation. The group concluded that the short  $T_E$  data was weighted toward blood volume, whereas the signal at the longer  $T_E$  reflected blood oxygenation.

In a conference abstract, Towse et al. (2009) underwent a quantitative study of the BOLD effect ( $T_R/T_E/\alpha=1000\text{ ms}/35\text{ ms}/60^\circ$ ) following brief contractions. By including NIRS and doppler ultrasound data, the group showed that the transient BOLD signal can be explained by the changes in blood volume and saturation.

## 3.2 Muscle functional magnetic resonance imaging

Although the BOLD effect is closely associated with functional magnetic resonance imaging (fMRI) in the brain, so-called muscle functional magnetic resonance imaging (mfMRI) studies do not typically exploit the BOLD effect. mfMRI most often involves  $T_2$ -weighted sequences to generate statistical parametric maps of areas indicating high  $T_2$  change, indicating muscle recruitment. A typical example is Price et al. (2003), examining muscle activation during plantar flexion at varying knee angles.

The BOLD method has an advantage over mfMRI in that the scan time is shorter, allowing better time resolution. BOLD effects are also easier to achieve with less intense exercise when compared with the mfMRI technique (Meyer et al. 2001).

One mfMRI study of potential interest to this project was performed by Nygren (2006), who examined the effect on  $T_2$  of exercise in patients with intermittent claudication. The study found that  $T_2$  increased in the gastrocnemius, while decreasing in the soleus immediately after exercise.

## 3.3 Arterial spin labelling

ASL is a technique for acquiring perfusion images without an external contrast agent. ASL was first described in 1992 by Williams et al., as a continuous labelling technique. They demonstrated cerebral blood flow (CBF) measurements in rats under hypercapnia, which had good agreement with the literature. They also demonstrated reduced perfusion to an induced injury in rat brain. The FAIR ASL technique was later described by Kim (1995). Functional maps generated from a finger movement paradigm were demonstrated.

ASL images of muscle were first acquired by Frank et al. (1999). The group used a CASL pulse sequence and reported quantitative values of perfusion during a dynamic plantar flexion exercise protocol. The data was analyzed using regions of interest (ROIs) of muscle groups in the lower leg, and the perfusion was found to be highly heterogeneous amongst muscle groups and between subjects.

The FAIR technique has been applied to muscle by Boss et al. (2006). The authors argue that the FAIR sequence, like other PASL techniques, offers lower specific absorption rate (SAR) than CASL techniques, and reduces the influence of magnetization transfer, arterial transit time, and variations in  $T_1$ . The study produced images

of the forearm after hand-gripping exercises, which showed increased perfusion in the muscle groups active during exercise. The measurements correlated well with the literature values, producing peak perfusion rates of up to  $221.6 \pm 44.2 \text{ml}/(\text{min} \cdot 100\text{g})$ .

Wu et al. (2008a) have used the CASL technique to characterize the flow in various muscle groups of the extremities, using an ischemia-reactive hyperemia paradigm. The study examined healthy muscle, and demonstrated significant flow heterogeneity amongst the muscles of the lower leg, foot and forearm. The variations in perfusion were attributed to fibre type differences. The group more recently presented a study using the CASL technique on patients with PVD at the International Society for Magnetic Resonance in Medicine (ISMRM) (Wu et al. 2008b). The study found a correlation of reduced blood flow and delayed flow response with the more severe categories of the disease, although the patients with less serious PVD did not vary significantly compared to the control group.

### 3.3.1 Combined BOLD with ASL

Since the BOLD signal can be affected by perfusion and blood volume in addition to oxygenation, a technique such as ASL, which is sensitive only to perfusion, is useful to help interpret BOLD images. Using ASL to supplement the BOLD technique was done in the brain as early as 1997, by Kim et al.. The study used a multi slice FAIR technique, and found that the relative BOLD and CBF changes were not correlated across subjects. Statistical parametric maps generated from the two techniques typically show similar results (Detre and Wang 2002).

At ISMRM 2008, Tan et al. presented preliminary results from a study with goals similar to this thesis. They used a spiral BOLD sequence in conjunction with a FAIR ASL sequence to study a patient with PVD and compared with healthy volunteers. The BOLD sequence had a train of four echoes which were used to generate a  $T_2^*$ -map. Their preliminary results suggested that the healthy volunteers experienced a greater increase in perfusion as a result of exercise compared to the patient with PVD. There was a small difference in the  $T_2^*$  as well, but it was unclear whether the difference was significant.

## 3.4 Fast acquisition techniques

### 3.4.1 Echo planar imaging

Although the spiral k-space trajectory may also be described as an echo planar technique, EPI typically refers to Cartesian, or near-Cartesian acquisition trajectories that cover k-space in a single echo. The first such trajectory was described by Mansfield (1977). His letter describes a pulse sequence in which one in-plane gradient is

held constant while the other has its polarity periodically reversed. The effect is a ‘zig-zag’ trajectory through k-space.

A modification to the EPI technique was described by Ljunggren (1983). The previously constant gradient was modified to periodically turn on for very short bursts in the same direction, during the switching time of the bipolar gradient. This has the effect of a piecewise horizontal traversal of k-space (see **figure 2.4**). The modified EPI technique was used in this study.

### 3.4.2 Spiral imaging

Although the technique had been described previously (Ljunggren 1983), images obtained using a spiral k-space trajectory were apparently first published by Ahn et al. (1986). Their method used linearly increasing sinusoidal gradient patterns, which resulted in a high degree of oversampling of the centre of k-space. Alternative approaches to the spiral trajectory were later proposed by Hardy and Cline (1989). Instead of choosing a constant angular speed, their trajectories are designed for optimum performance under the constraints of a scanner’s gradient amplitude and slew rate.

Glover (1999) has calculated an analytical approximation to the ideal spiral trajectory that saves calculation time when the scan is run. The increase in gradient amplitude is proportional to  $t^{2/3}$ , which lessens the non-uniformity of the k-space sampling but does not eliminate it (see **figure 2.6** on page 17). Glover and Li have experimented with various spiral schemes for improved SNR and reduced susceptibility effects, including spiral in-out (Glover and Law 2001), and spiral in-in (Li et al. 2006).

# Chapter 4

## Problem definition and hypothesis

### 4.1 Problem definition

Ziegler-Graham et al. (2008) estimate that there were 1.6 million people living with amputations in the United States in 2005, 38% of whom had both peripheral vascular disease (PVD) and diabetes mellitus. Looking to the future, they say,

*“Even assuming that age-, sex-, and race-specific rates of both diabetes and diabetes-related amputations remain unchanged, the number of people with diabetes who are living with the loss of a limb will nearly triple by the year 2050.”*

The authors go on to assert that obesity rates are increasing, which indicates that the numbers could be higher.

The standard tests for PVD described in section 1.2.1 leave room for improvement. The walking test is unreliable because it fails to consistently distinguish the various grades of PVD (Peräkylä et al. 1998; Labs et al. 1999). The post-exercise ABI test reliably indicates the presence of PVD (Peräkylä et al. 1998). The technique is limited by the fact that it provides no spatial information on the severity of the disease along the leg or amongst different muscles. Spatial information is important for determining treatment.

### 4.2 Proposed solution

Given that MRI is a particularly effective tool for the functional imaging of soft tissue, an MRI solution to the problem of PVD assessment is proposed. The BOLD signal in muscle has previously been shown to vary during ischemia-reactive hyperemia trials (Ledermann et al. 2006b), and pre- post-exercise tests (Noseworthy et al. 2003). The ASL signal has also been shown to vary under such conditions (Frank et al. 1999).

Exercise is more natural, and more physiologically relevant than ischemia-reactive hyperemia for perturbing muscle perfusion and oxygenation. The exercise must be done in the magnet, however, to acquire the critical data immediately after the completion of the exercise; some physiological effects dissipate in less than one minute. This requires the construction of an MRI compatible ergometer, which will be used to standardize the exercise.

It is expected that the physiological response to exercise will differ between healthy and diseased individuals, and that the difference will be apparent using the BOLD and ASL techniques. The confounds to the measurement may include:

- motion, which may cause  $B_0$  and  $B_1$  field changes
- blood pressure, pulsatility
- food and drug intake including caffeine
- fitness level, age, gender

The data will be collected and plotted as a time-series. First, optimal scan parameters must be determined for the BOLD and ASL techniques. The optimum k-space acquisition type must also be determined. Next, an exercise program to properly challenge the muscles must be developed. Then the muscle perfusion can be quantified using ASL. Finally, a scheme can be developed that uses the perfusion data to complement the BOLD data and give a reliable assessment of vascular health.

Once the development work is completed, a future project can use the technique to examine patients with PVD. From previous studies, a reduced percent BOLD signal change is expected in people with PVD (Ledermann et al. 2006b). The recovery of the signal is also expected to be delayed in time.

### 4.2.1 Hypothesis

It is already understood that ASL and BOLD can be used to monitor physiological changes in muscle. It is hypothesized that these methods can be made more robust by choosing the optimal sequence type and by taking into consideration, and correcting for, motion.

# Chapter 5

## Motion confound to functional imaging of skeletal muscle

### 5.1 Introduction

This experiment used exercise as a means to affect the blood oxygenation, since it is relatively safe, less painful than ischemia, and has proven effective at eliciting BOLD and ASL signal changes (Meyer et al. 2004) in muscle. Although BOLD data has been collected immediately after single flexion exercise (Damon et al. 2007a,b), data collected during exercise may provide insight into the condition of the microvasculature.

Unfortunately, the motion associated with imaging during exercise may be problematic for image registration, which is required to do GLM BOLD time series analysis, as is done in brain imaging studies. This experiment set out to study the impact of motion on such data.

### 5.2 Materials and methods

#### 5.2.1 Acquisition hardware

All data was collected on the MRI scanner dedicated to research at the Imaging Research Centre of St Joseph's Healthcare Hamilton. The scanner is a 3 Tesla GE HD Signa MRI, which includes eight independent receiver channels (GE Healthcare, Milwaukee, WI). For this experiment, the body RF coil was used for excitation, and acquisition was done with a single channel receive-only flexible surface coil.

### 5.2.2 Scanning sessions

The data was acquired in two separate scan sessions. The sessions both began with a three plane localizer, followed by an axial  $T_1$ -weighted FSPGR anatomical with  $T_E/T_R/\alpha=5\text{ms}/51\text{ms}/19^\circ$ . Ten 5 mm thick, axial slices were acquired in the lower leg with a 256x256 matrix and a 16 cm FOV. BOLD data collection followed, with a gradient echo EPI pulse sequence with  $T_E/T_R/\alpha=35\text{ms}/2\text{s}/90^\circ$ . Geometric parameters were the same as the anatomical, except for a 64x64 matrix (interpolated to 128x128). 180 time points were acquired, for a total scan time of 360 s.

The first session included two types of motion of the leg, without exercise. A twisting motion and a through-plane translation were performed. The twist paradigm was a small rotation of the lower leg at  $t=30$  s, then a return to the original position at  $t=60$  s, twisted again at  $t=90$  s, and so on. The magnitude of the twist was approximately  $4^\circ$ . The translation paradigm was similar in that the position of the leg was changed and then returned at 30 second intervals, except the motion was a through plane shift of about 5 mm (1 voxel). No exercise was performed during these motion sessions.

The exercise paradigm was 30 s rest, followed by 30 s of isometric plantar flexion exercise, with six repetitions as in the motion paradigms. A calibrated elastic band, known as a Thera-Band (The Hygenic Corporation, Akron, Ohio) was used for resistance.

### 5.2.3 Motion correction

A custom-coded motion correction script was developed, based on the FLIRT tool from the FSL package (<http://www.fmrib.ox.ac.uk/fsl>) (Smith et al. 2004; Woolrich et al. 2009). The script allowed the use of the `-refmask` option, which allowed the weighting factors to be applied to certain areas of an image so that some parts will be registered preferentially over others. This allowed the arteries to be masked out of the image for registration purposes. The arteries are problematic because they are bright, which causes them to be preferred by the registration algorithm, but they move due to pulsatile flow. The script also allowed in-plane registration using either three or five degrees of freedom (DOF). Three DOF performs registration using in-plane translations and rotations only, while five DOF adds in-plane scale factors. The script is reproduced in appendix A.

### 5.2.4 Analysis

The data was analysed with FSL's FEAT tool, using a square wave based ideal model. The model shape is shown above the plot in **figure 5.9**. The BOLD exercise and

motion data was fit using the GLM to generate statistical parametric maps for the lower leg images.

### 5.3 Results and Discussion

Sample BOLD data results from the exercise paradigm are shown in **figure 5.9**. Following statistical analysis with FEAT, anti-correlation in the medial gastrocnemius was found with a low/high square wave based model (i.e. signal intensity was initially high). The red-yellow colour-scheme indicates correlation ( $P < 0.05$ , uncorrected) to a low/high type model, and the dark-light blue scale is anti-correlation, or correlation to a high/low type model. The time-series of an anti-correlated pixel is also shown. The signal is reduced during exercise, presumably caused by a decrease in the ratio of oxyHb to deoxyHb. The signal intensity of the rest phases also show a slight increase over time, likely due to increased perfusion.

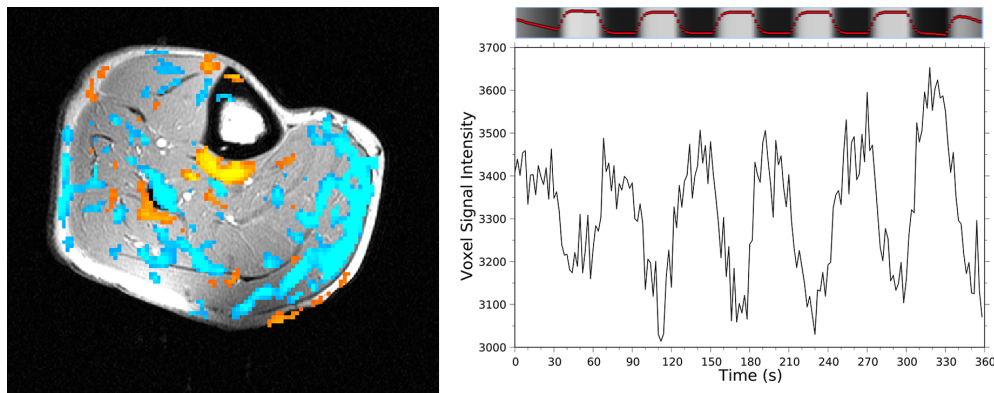


**Figure 5.9: Isometric exercise.** Warm colours indicate correlation to a square wave based low/high type model. Cool colours are anti-correlated. Many pixels of the medial gastrocnemius are anti-correlated, as may be expected from plantar-flexion exercise. The time-series is from a highly anti-correlated pixel in the gastrocnemius.

The through-plane shift paradigm tended to produce anti-correlation over the whole cross-section of the leg, as shown in **figure 5.10**. Given that the muscles likely to be recruited in the exercise and those of the anterior compartment showed similar responses, the data is identifiably corrupted. This is advantageous, since motion of this type is unlikely to be confused with BOLD data from a physiological origin.

Sample BOLD data from the twist paradigm is shown in **figure 5.11**. The plot shows the time series of a voxel in the gastrocnemius, which has the same characteristic square wave shape as the exercise data shown in **figure 5.9**. Compared to

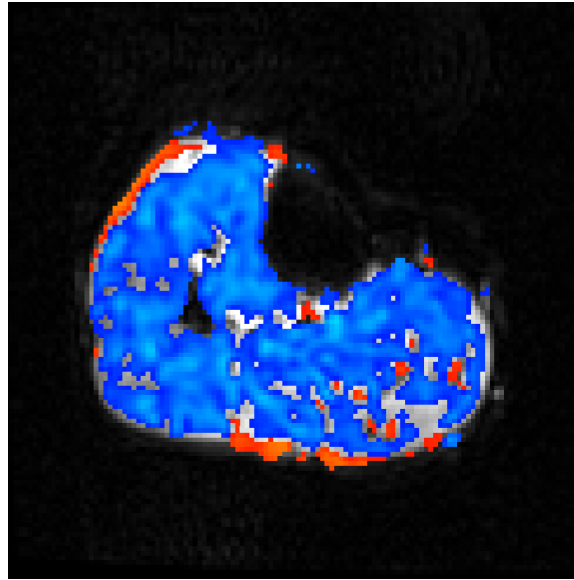


**Figure 5.10: Through-plane shift parametric map.** The map shows a high level of anti-correlation across the leg, which reveals that the signal is not related to physiological changes.

the exercise data, the twist data may actually be a better fit to a square wave type model, since the transitions are sharper. This occurs because bright voxels are simply shifted into the location of darker ones, and then shifted back. After statistical analysis with FEAT, there was a strong correlation in these pixels with the square wave based model. The correlated regions became broader when increased smoothing was applied to the image before applying the model, as is commonly practised. Cluster thresholding did not eliminate the large areas of correlation.

After performing motion correction with the script in appendix A, the twisting motion appeared to be eliminated from the data set, leaving only small non-linear geometric distortions. When FEAT analysis was performed on the motion corrected data, however, the correlation still existed, but was confined to certain areas of the leg, mimicking single muscle activation data. An example with 5.0 mm full width at half maximum (FWHM) gaussian smoothing and cluster filtered thresholding to  $P < 0.05$  is shown in **figure 5.11**.

## 5.4 Conclusions

It is not hard to imagine an in-plane twisting motion of  $4^\circ$  being introduced during plantar- or dorsi-flexion of the foot. This motion must be eliminated during MR experiments where image data is acquired during exercise. Even with linear in-plane

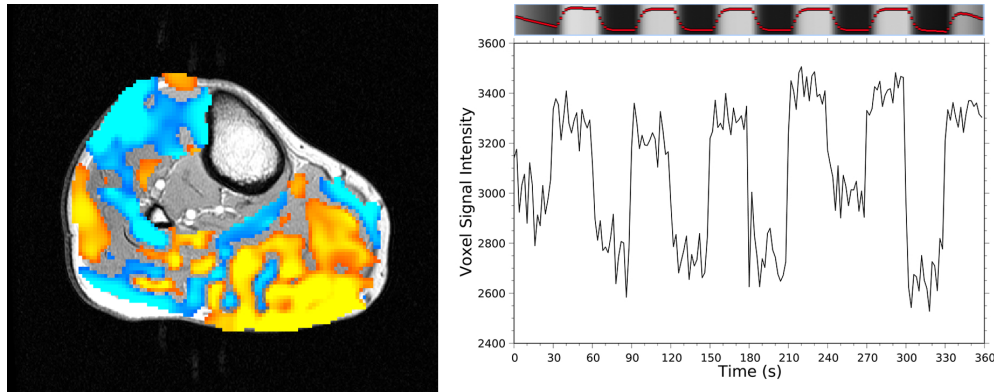


**Figure 5.11: Twisting motion.** As earlier, warm and cool colours indicate correlation and anti-correlation, respectively. Broad areas of correlation were found, which remained even after the motion had apparently been eliminated from the data set using registration. The time-series is from a highly correlated pixel in the gastrocnemius.

motion correction, complete removal of artifacts was not possible. Compared to the exercise data of **figure 5.9**, the twisting data of **figure 5.11** shows both strongly correlative and strongly anti-correlative behaviour. Because of this, BOLD data obtained during exercise should be examined for display of these complementary regions. The signal of correlated or anti-correlated voxels can also be examined for the sharp, non-physiological transitions similar to those of the twisting data set. Data sets that show such behaviour should be closely examined for motion, to be sure the BOLD signal intensity changes have a physiological basis. Motion based signal intensity changes may mask or mimic the true change in BOLD signal, leading to incorrect conclusions regarding oxygenation or perfusion of muscles during exercise.

## 5.5 Force standardization and motion elimination

In order to achieve valuable results, the force applied or the amount of work performed by the subject must be repeatable. In physiological testing, a device with an adjustable resistance for calibrating the work performed is known as an ergometer. The ergometer for this study had to be simple to operate, and constructed from non-ferromagnetic materials so that it was compatible with the MRI scanner. The device also had to be comfortable for patients, to increase compliance during many repetitions of the exercise protocol. Finally, the device had to minimize patient motion during the scan to prevent image artifacts.

### 5.5.1 Ergometer

The initial ergometer designed and built was a foot-pedal type device for plantar flexion contractions (calf-raise type exercise). The device used a Thera-Band for resistance. A schematic of the ergometer is shown in **figure 5.12**, with a photo in **figure 5.13**. As the initial Thera-Band and pedal positions were fixed, resistance to muscle contraction was calibrated by varying the relaxed length of the band. Since this adjustment was somewhat cumbersome and time consuming, the resistance was modified according to subject body mass, as opposed to measured strength.

In order to standardize the motion of the subject's foot, a portion of an ankle-foot orthosis was used. The subject's foot was firmly strapped into the orthosis with padding, and the motion of the orthosis was limited by the device to a single plane. The pivot point was made as close as possible to the subject's ankle, to minimize discomfort and unnecessary motion of the leg. Stops were added to standardize the leg position at the extremes of the motion. This ergometer was used for all experiments described in the following chapters.

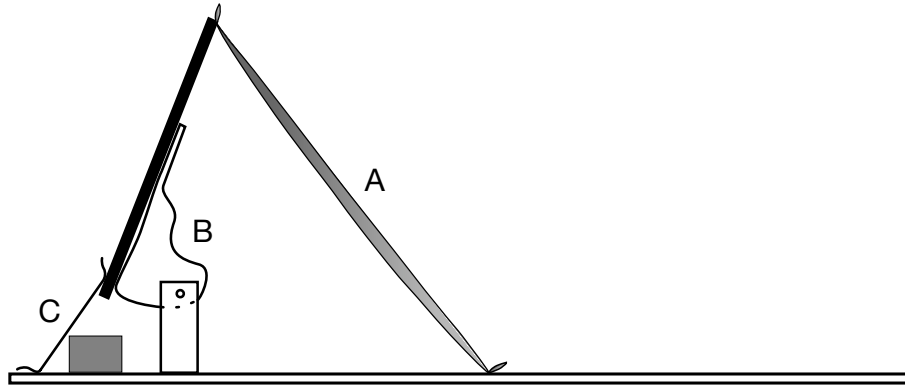


**Figure 5.12: Elastic ergometer schematic.** This ergometer used an elastic Thera-Band (A) for resistance to plantar flexion. The subject's foot was placed in a modified ankle-foot orthosis (B), which pivoted on a screw near the ankle. Stops were added in the form of a block and a nylon strap (C), to standardize the leg locations in the flexed and rest positions, respectively.



**Figure 5.13: Elastic ergometer photo.** Thera-Bands are set for resistance, and the flexible surface coil is ready to accept a subject's leg.



# Chapter 6

## Comparison of echo planar and two shot spiral in-out imaging

As noted in section 2.4, BOLD imaging requires a fast acquisition method to achieve adequate time resolution. Two such fast acquisition methods are spiral imaging and echo planar imaging (EPI). Previous work has shown advantages of spiral, when compared to EPI, for brain fMRI studies (Klarhöfer et al. 2002; Yang et al. 1998; Sangill et al. 2006). Spirals are relatively insensitive to motion, typically produce higher signal, and spiral in-out is robust to susceptibility artifacts. Nevertheless, EPI remains the more common technique. The lower leg has unique challenges due to susceptibility effects caused by the long bones, shimming difficulties, and motion. The goal of the current study was to compare spiral and EPI acquisition for muscle BOLD imaging during exercise.

### 6.1 Materials and methods

#### 6.1.1 Acquisition hardware

All data was collected on the MRI scanner dedicated to research at the Imaging Research Centre of St Joseph's Healthcare Hamilton. The scanner is a 3 Tesla GE HD Signa MRI, which includes eight independent receiver channels (GE Healthcare, Milwaukee, WI). The body coil was used for excitation, and acquisition was done with a single channel receive-only flexible surface coil. The scanner is a twin speed model, meaning it includes two gradient sets: *zoom* and *whole*. Although the *zoom* gradients are rated for higher performance in terms of gradient amplitude and slew rate, the *zoom* system is more prone to non-linearity across the volume of interest by a factor of 10 (Wang et al. 2004). The *zoom* gradients were found to produce a visible increase in the artifacts associated with the spiral scans (data not shown), so

the *whole* gradient system was used for spiral imaging.

### 6.1.2 Scanning sessions

The leg imaging sessions began with a three plane localizer, followed by two axial  $T_1$ -weighted FSPGR anatomicals ( $T_E/T_R/\alpha=5\text{ms}/51\text{ms}/19^\circ$ ), one in the rest position and one in the flexed position. Three 10 mm thick axial slices were acquired from the right leg calf muscles with a  $256 \times 256$  matrix. BOLD ( $T_E=40\text{ms}$ ) imaging followed, with identical geometry, but a  $64 \times 64$  matrix (spiral reconstructed to  $128 \times 128$ ). A  $T_R$  of 500 ms was used in order to acquire multiple slices with a high temporal resolution. Using a published value for muscle  $T_1$  of 900 ms at 3.0 Tesla (de Bazelaire et al. 2004), a flip angle of  $55^\circ$  was used to maximize the BOLD signal according to equation 2.13 (see figure 2.2 on page 12).

The order of EPI and spiral imaging was randomized amongst the subjects. Although both dynamic (gated) and isometric exercise paradigms were used, only the isometric data will be discussed here, since it is more straightforward to interpret. The exercise paradigm was an initial 30 second rest period, followed by three cycles of 30 second moderate, body-mass adjusted, isometric, plantar flexion contractions with 1 minute rest periods.

### 6.1.3 Spiral imaging

The spiral sequence used in this study is based on the method of Hardy et al., and the reconstruction was done off-line using the method of Meyer et al. (1992). The spiral sequences are slew rate limited, and were provided by Dr. Gary Glover (Department of Radiology, Stanford University, Stanford, California, USA). The increase in gradient amplitude is proportional to  $t^{2/3}$ , which reduces, but does not eliminate, the non-uniformity of the k-space sampling (see figure 2.6 on page 17).

When acquiring single-shot spiral images, some images were unacceptable for analysis due to large ring artifacts and decreased signal in areas near the bone-tissue interface. The pulse sequence used is capable of a spiral in-out acquisition, with multiple interleaves. A comparison of the sample images from various acquisition strategies is shown in **figure 6.14**. For these images, a slice superior to the bulk of the calf muscle was intentionally selected for its high bone content, to ensure some inhomogeneity in the  $B_0$  field.

Based on the spiral images it was decided that *two shot spiral in-out* acquisition provided the best compromise for acceptable image quality with the fastest possible time resolution. The pulse sequence producing this trajectory is shown in **figure 6.15**.

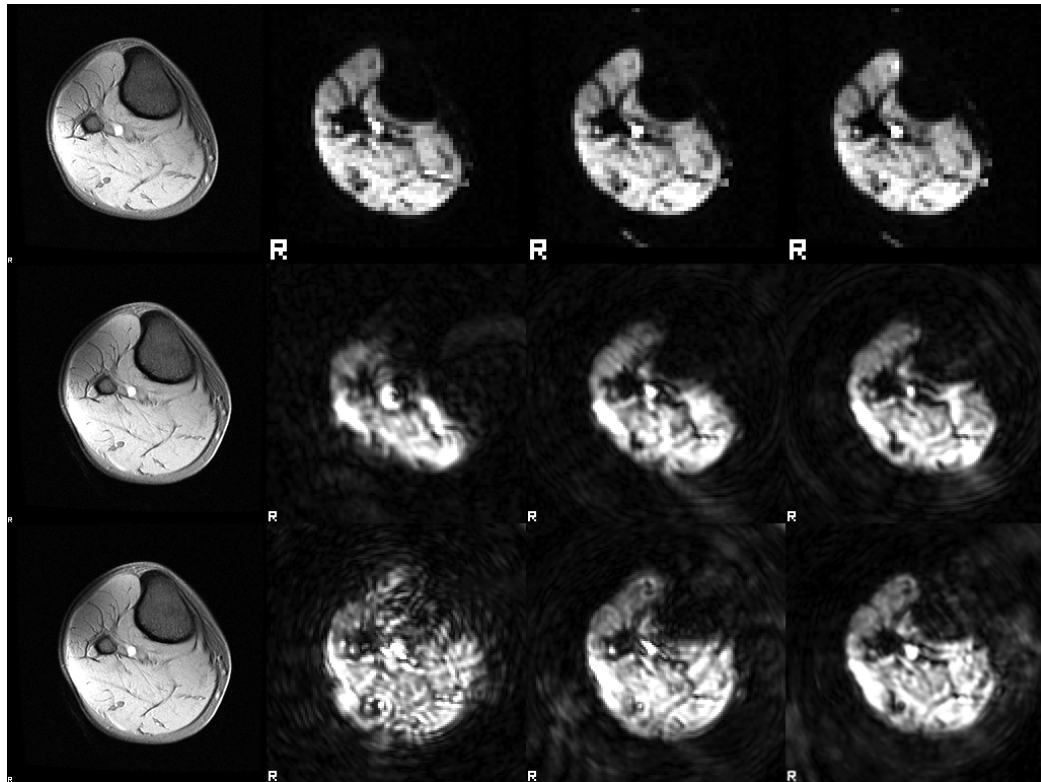


**Figure 6.14: Multi-shot comparison.** **Top row:** Anatomical and EPI images – single shot, two shots, and four shots, from left to right. **Middle row:** Anatomical and spiral out images – single shot, two interleaves, and four interleaves, from left to right. **Bottom row:** Anatomical and spiral in-out images – single shot, two interleaves, and four interleaves, from left to right.

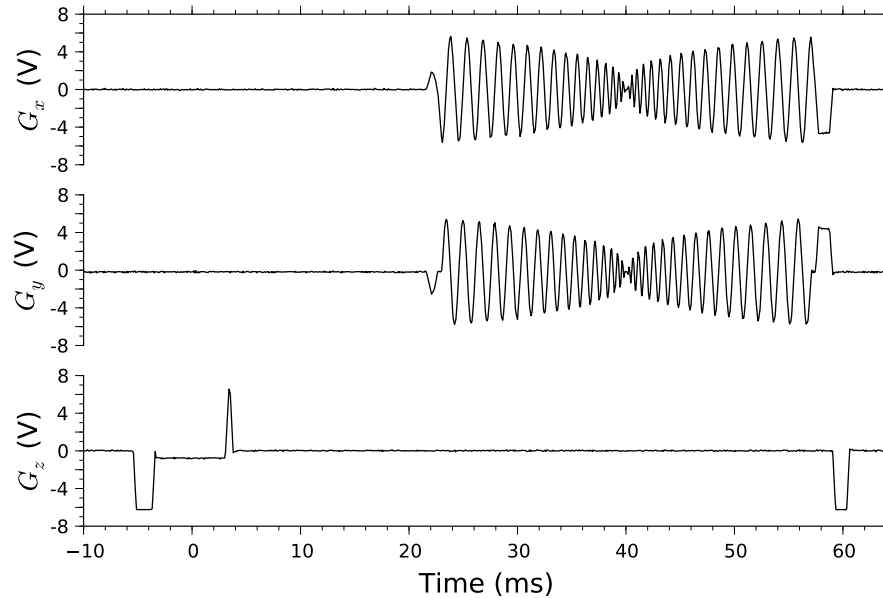


**Figure 6.15: Spiral in-out pulse sequence.** This sequence shows a two interleaved acquisition, so the spatial encoding time for each spiral is shortened. Note that both spirals sample the centre of k-space at the  $T_E$  of 40 ms.

#### 6.1.4 Echo planar imaging

Since the spiral acquisition used two interleaves, it was initially decided that a two shot EPI acquisition would be used for consistency. As noted in section 2.4.1, however, multi-shot EPI can be problematic when bulk motion is present between the partial k-space acquisitions. **Figure 6.16** is an image series showing two shot EPI images acquired during an exercise scan, with increasing severity of the out-of-phase artifact. Complex correction techniques are needed for the artifacts associated with multi-shot EPI, which were not in the scope of this project (Robson et al. 1997). As a result, and because the advantages of multi-shot EPI were not dramatic, a single shot EPI acquisition was used.

#### 6.1.5 Subjects

Data was collected from three males with ages  $26 \pm 3$  years. The subjects were well rested for at least a day in advance, had not consumed food or caffeine for at least two hours prior to scanning, and were non-smokers. ROI analysis was performed using AFNI (Cox 1996) to obtain image time-course signal changes from the medial and lateral gastrocnemius (MG and LG), soleus (SOL), lateral compartment (LAT), and

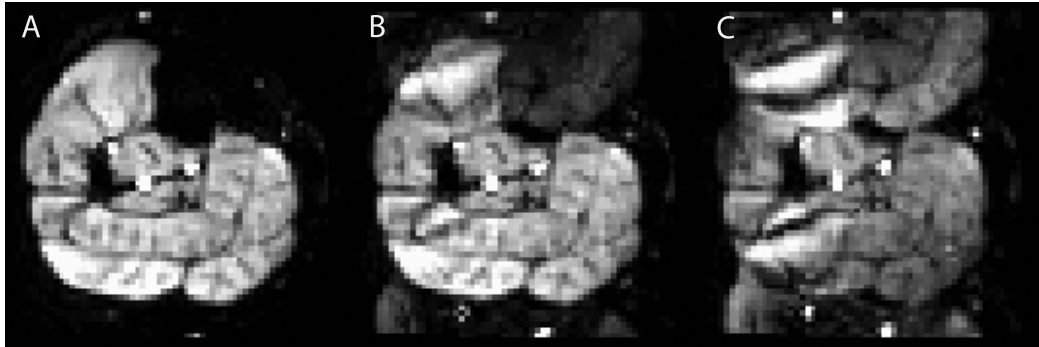


**Figure 6.16: Multi-shot EPI artifact.** Image (A) is relatively noise and artifact free, illustrating the potential of multi-shot EPI for undistorted, high SNR images. (B) and (C) show images later in the series with increasing severity of the out-of-phase artifact caused by bulk motion between the acquisitions.

anterior compartment (ANT), shown in **figure 1.1** on page 4.

## 6.2 Results and discussion

Sample images using the EPI and *two shot spiral in-out* acquisitions are shown in **figure 6.17**. EPI appears to produce a sharper image, as demonstrated by the fact that most of the subject's skin is resolved. The SNR appears much better in the EPI image as well.

Differences in the geometries of the two scans are apparent, especially in the region of the anterior compartment. It was noted in section 2.4.1 that the distortion due to off-resonance effects in an EPI image is a warping in the phase encode direction. This is evident in **figure 6.18**. The EPI has a distortion problem on the left of the image, where it is evident that the outline of the muscle is shifted in the anterior direction. While not perfect, the spiral generally shows good fidelity to the anatomical image.

The obtained signal time courses for each muscle or muscle group were normalized to the initial rest portion of the data. Cubic spline fits were performed on the initial recovery portion of the rest data, as shown in the sample data of **figure 6.19**. The recovery signals included spin saturation effects for several time-points due to bulk motion during the contraction, which were ignored. The signals were characterized by the base-peak height of the normalized signal change during the hyperemic recovery curves, from the lowest to highest points. This change has been found to be correlated with exercise intensity (Wigmore et al. 2004). The results are shown in **table 6.4**. All values are  $\times 10^{-2}$  of the normalized signal intensity for each muscle group. The values for each subject and muscle group were averaged over the three recovery periods, and

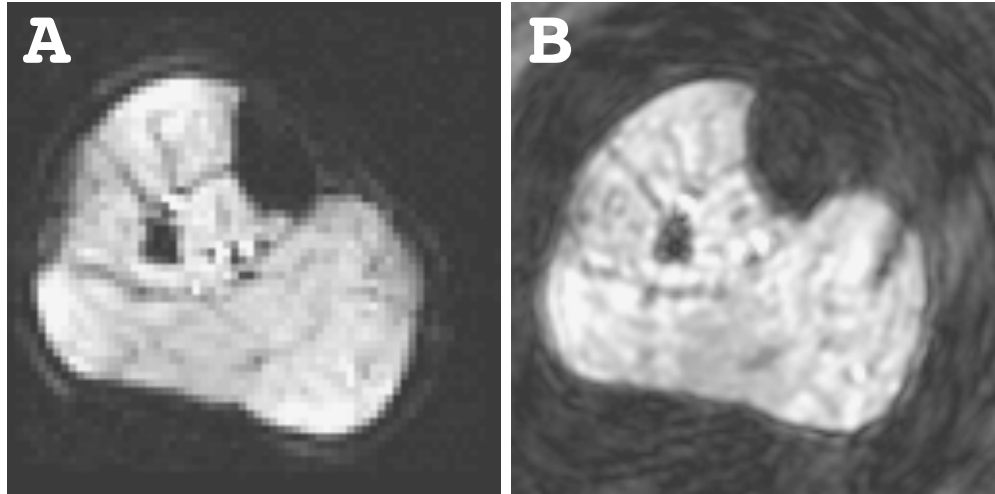


**Figure 6.17: EPI and spiral image results.** Axial BOLD images of the lower leg, using (A) EPI and (B) *two shot spiral in-out* acquisition. The SNR appears significantly better in the EPI image.

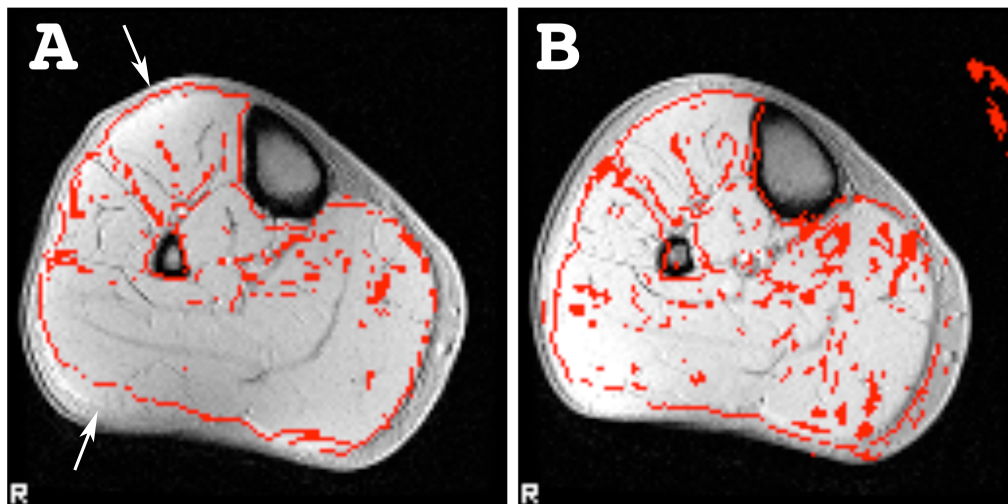


**Figure 6.18: EPI and spiral geometry comparison.** BOLD image outlines (red) overlaid on anatomical images of the lower leg, using (A) EPI and (B) *two shot spiral in-out* acquisition. The EPI outline reveals a distortion in the phase encode (vertical) direction, especially near the anterior compartment and the lateral gastrocnemius (white arrows).

the standard deviation is also given. N/A indicates the absence of a recovery peak, and PA indicates a pulsatility artifact that prevented measurement.

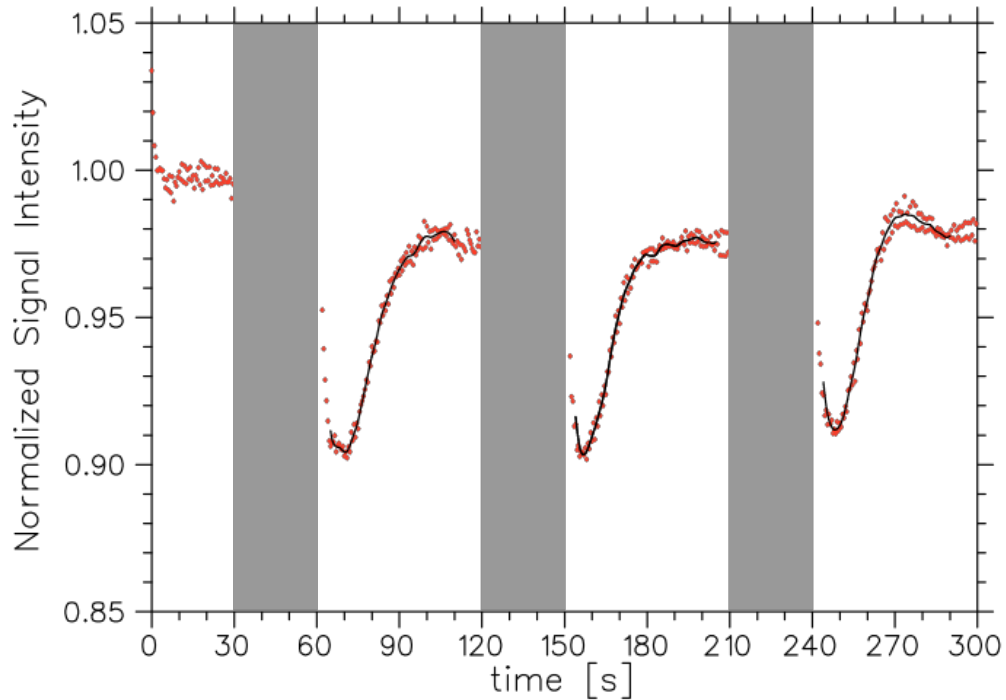


**Figure 6.19: BOLD signal time course.** EPI BOLD signal intensity (red) in the MG muscle from subject 1, normalized to the initial rest period. Three 30 second isometric contractions (grey bars) were followed by 60 second recovery periods. Cubic spline fits (black lines) were used to calculate the base-peak signal change of the hyperemic recovery curves.

The results show that the *two shot spiral in-out* acquisition typically had increased variability compared to the single shot EPI. This is evident in the MG and LAT results, which are very important to plantar flexion. Furthermore, in the soleus of subject three, the spiral artifacts obscured the muscle to such an extent that ROI analysis was not appropriate. A study examining plantar flexion can not afford to sacrifice data from the soleus muscle, since the muscle is primarily made of slow oxidative fibres, allowing comparison to the gastrocnemius.

### 6.2.1 Spiral weighting schemes

Given that the spiral acquisition included spiral-in and spiral-out for every echo, two images are generated which must be combined. Glover et al. have suggested that a

**Table 6.4:** EPI and spiral BOLD signal change

	Subject 1		Subject 2		Subject 3	
SNR	62	10	106	19	44	21
Muscle	EPI	Spiral	EPI	Spiral	EPI	Spiral
MG	$7.40 \pm 0.09$	$9 \pm 2$	$4.6 \pm 0.4$	$3 \pm 1$	$6 \pm 1$	$6.1 \pm 0.6$
LG	N/A	N/A	$4.1 \pm 0.4$	$3.8 \pm 0.6$	N/A	N/A
SOL	$2.7 \pm 0.4$	$3.1 \pm 0.1$	$4 \pm 2$	$2.9 \pm 0.8$	$2.5 \pm 0.8$	PA
LAT	$9.03 \pm 0.09$	$9 \pm 2$	$4.9 \pm 0.1$	$4.5 \pm 0.1$	$3.4 \pm 0.4$	$4 \pm 2$
ANT	$2.4 \pm 0.2$	$2 \pm 1$	$1.7 \pm 0.9$	$0.9 \pm 0.5$	N/A	N/A

All values  $\times 10^{-2}$ ; PA: artifact prevented measurement; N/A: No visible recovery peak

weighted average be used to maximize the signal throughout the image (Glover and Law 2001). The scheme, which will herein be called the maximum-weighted scheme, involves multiplying the spiral-in and -out signals,  $s_i$  and  $s_o$  respectively, by their contribution to the overall signal,  $s_w$ , as follows:

$$s_w(\mathbf{r}) = \left( \frac{s_i(\mathbf{r})}{s_i(\mathbf{r}) + s_o(\mathbf{r})} \right) \cdot s_i(\mathbf{r}) + \left( \frac{s_o(\mathbf{r})}{s_i(\mathbf{r}) + s_o(\mathbf{r})} \right) \cdot s_o(\mathbf{r}) \quad (6.20)$$

One can also define a minimum-weighted scheme, with the objective of minimizing the signal intensity everywhere, including the noise:

$$s_w(\mathbf{r}) = \left( \frac{s_o(\mathbf{r})}{s_i(\mathbf{r}) + s_o(\mathbf{r})} \right) \cdot s_i(\mathbf{r}) + \left( \frac{s_i(\mathbf{r})}{s_i(\mathbf{r}) + s_o(\mathbf{r})} \right) \cdot s_o(\mathbf{r}) \quad (6.21)$$

Finally, a simple average of the two signals can be employed:

$$s_w(\mathbf{r}) = \frac{1}{2} \cdot s_i(\mathbf{r}) + \frac{1}{2} \cdot s_o(\mathbf{r}) \quad (6.22)$$

The three weighting schemes were employed on an average of the first 25 images from the *two shot spiral in-out* dataset of subject 1. The SNR was calculated, with the results summarized in **table 6.5**. The calculated SNR differs slightly from the previous table because different ROIs were used. It is evident that the choice of weighting scheme greatly affects the calculated SNR. While the mean signal from the ROI was virtually unchanged across the weighting schemes, differing by only 1%, the calculated SNR values increased by 67%. Still, the SNR values do not compare to that of the EPI scan, which was 62 in this subject.

**Table 6.5:** Weighting scheme results

Image	Mean Signal	Background SD	SNR
Maximum	1163.06	96.50	12
Average	1155.93	68.67	17
Minimum	1148.80	56.06	20
Spiral-in	1124.45	58.65	19
Spiral-out	1187.42	122.01	10

## 6.2.2 K-space navigation

While the spiral in-out trajectory has intuitive appeal, since both spirals sample the centre of k-space at the echo time, it has recently been suggested by Li et al. that spiral in-in provides the best signal where off-resonant spins are present (Li et al. 2006). The authors argue that for off-resonant spins, the true centre of k-space is offset from the expected value. This means that, if the second spiral is a spiral-out, the centre of k-space may not be sampled until very late in the acquisition, when much of the signal has been lost to  $T_2^*$  decay. Although the location of the true centre of k-space for the off-resonant spins is not known, the argument is that the spiral-in will more likely acquire the true centre early in the trajectory.

## 6.2.3 Concomitant field effects

Concomitant magnetic fields,  $B_c$ , are higher-order spatially varying fields created secondarily to the actions of the gradients. They can cause artifacts by introducing additional phase shifts according to:

$$\phi_c(t) = \int_0^t B_c dt' \quad (6.23)$$

The concomitant field effects are not expected to be large for this study, since the acquired slices were all at or near the isocentre of the magnet. For a 2D axial scan, the concomitant field varies according to  $z^2$ , as follows (King et al. 1999):

$$B_c = \left( \frac{g_x^2(t) + g_y^2(t)}{2B_0} \right) z^2 \quad (6.24)$$

## 6.3 Conclusions

*Two shot spiral in-out* acquisition was shown to be far superior to single shot spiral. Compared to the EPI, the two shot spiral images typically had higher overall signal, and better geometric fidelity. The EPI distortion, however, was merely a slight shift in the anterior direction, which may be corrected using separately acquired field-maps (Jezzard and Balaban 1995). EPI had higher SNR, at  $70 \pm 30$  compared to spiral with  $17 \pm 6$ . Furthermore, because the quality of the single-shot EPI was adequate, EPI had twice the time resolution of the two-shot spiral. The EPI produced slightly more reproducible results as well, with lower standard deviations on the base-peak signal changes.

It should be noted, however, that the spiral-out acquisition has an important advantage over the EPI sequence used in this study, namely short echo times. Short  $T_E$  is needed for  $T_1$ -weighted scans, as used in ASL. The EPI sequence described here acquires the centre of k-space half way through the acquisition time, so the minimum  $T_E$  afforded by the EPI sequence is about 25 ms.

# Chapter 7

## Arterial spin labelling development

### 7.1 Introduction

Given that the BOLD signal is sensitive to perfusion and blood volume as well as oxygenation, the signal is hard to interpret. Since arterial spin labelling (ASL) measures perfusion alone, the technique was attempted as a means to supplement the BOLD data, and enable a physiological interpretation to the signal changes. The technique was attempted first in a conventional functional brain imaging experiment, in order to validate the method and the image reconstruction. Following successful tests in brain, the technique was attempted in the lower leg.

### 7.2 Materials and methods

#### 7.2.1 Acquisition hardware

All data was collected on the MRI scanner dedicated to research at the Imaging Research Centre of St Joseph's Healthcare Hamilton. The scanner is a 3 Tesla GE HD Signa MRI, which includes eight independent receiver channels (GE Healthcare, Milwaukee, WI). For the brain studies, excitation and acquisition were done with an eight receiver channel head coil, with excitation done using the body RF coil. For the leg studies, the body coil was used for excitation, and acquisition was done with a single channel receive-only flexible surface coil.

#### 7.2.2 Pulse sequence

A FAIR ASL pulse sequence was acquired from Dr. Tie-Qiang Li (Department of Medical Physics, Karolinska Institute, Stockholm, Sweden) along with a program for reconstructing the data from raw form (P-file) to 16-bit (short integer) raw images.

The sequence uses a spiral acquisition method, and also includes features such as a sequence for  $T_1$ -mapping (Look and Locker 1970), and interleaved ASL-BOLD scanning.

In order to work with the data using standard functional analysis packages such as AFNI and FSL (Cox 1996; Smith et al. 2004), the images had to be converted to a single 4D volume file format. The NIfTI file format was chosen since it is compatible with both packages. Images from the eight receivers were combined using root-mean-squared (RMS) addition (Roemer et al. 1990).

### 7.2.3 Brain imaging

The brain imaging sessions began with a three plane localizer and included both BOLD and ASL sequences, as well as a 3D FSPGR 512x512 anatomical giving full brain coverage ( $T_E/T_R/\alpha=2.1\text{ms}/9.0\text{ms}/12^\circ$ ). The sessions also included susceptibility weighted imaging (SWI),  $T_1$ -map and GRE magnitude and phase sequences, which were not used for this project. The BOLD data was acquired with  $T_E/T_R/\alpha=35\text{ms}/2\text{s}/90^\circ$ , and the imaging volume was thirteen 4 mm thick slices with 1 mm gaps, acquired at 64x64 with a 24 cm FOV. The ASL data was acquired with  $T_E/T_R/\alpha=6.7\text{ms}/2\text{s}/90^\circ$ , and identical geometry to the BOLD, except that it was reconstructed to 128x128. The total scan time to acquire both labelled and unlabelled ASL images (one subtraction image) was therefore 4 seconds. The  $T_1$  for the ASL sequence was 1200 ms (Koziak et al. 2008).

During BOLD and ASL scanning, the subject performed an alternating hand motor task (finger-tapping), beginning with the right hand. The BOLD paradigm alternated every 30 seconds, repeating the cycle six times, for a total scan time of six minutes. The ASL paradigm alternated every 32 seconds, repeating the cycle four times, for a total scan time of 4 minutes, 16 seconds.

### 7.2.4 Leg imaging

The ASL technique was then applied to the lower-leg during exercise. The leg imaging sessions began with a three plane localizer, followed by an axial  $T_1$ -weighted FSPGR anatomical ( $T_E/T_R/\alpha=5\text{ms}/51\text{ms}/19^\circ$ ). Three slices of ASL data were acquired, at 64x64 (interpolated to 128x128), with a 16 cm FOV,  $T_E/T_R/\alpha=6.7\text{ms}/2\text{s}/90^\circ$  and  $T_1=1200$  ms. During ASL scanning, the subject performed 32 second isometric contractions, alternated with 56 second rest periods, with a 120 second rest period at the end.

## 7.3 Results and discussion

### 7.3.1 Brain imaging

Image acquisition and reconstruction was successful in the brain, as shown in **figure 7.20**. As expected, the labelled and unlabelled images are virtually indistinguishable with the naked eye, but the subtraction image shows higher perfusion in grey matter than white matter.

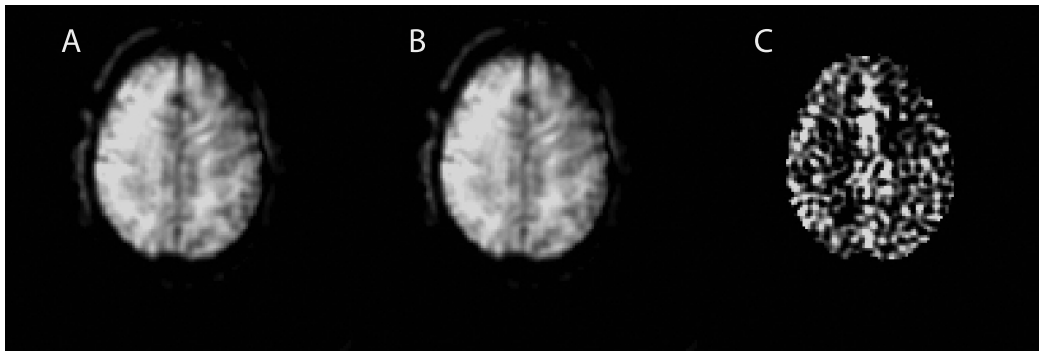


**Figure 7.20: Brain ASL Images.** Images results from brain imaging using the FAIR sequence: **(A)** Labelled image, **(B)** Unlabelled image, **(C)** Subtraction image, with signal proportional to perfusion. The subtraction image has been masked to remove artifacts outside the brain.

Correlation coefficient maps were generated from the functional data using square wave models, and are shown in **figure 7.21**. The maps were both thresholded to 0.32 (two tailed  $P < 0.01$  for 64 ASL samples, and  $P < 1.2 \times 10^{-5}$  for 180 BOLD samples). Cluster filtering was also applied using a nearest-neighbour threshold of 4 voxels.

The ASL technique was successful in the brain, resulting in high quality statistical parametric maps that closely matched those from the BOLD scans. Both techniques produced activation in the primary motor cortex (Hlushchuk and Hari 2006), but activated areas are not expected to precisely overlap, since the BOLD signal comes from predominantly the venous side, whereas the dominant signal source from ASL activation is on the arterial side.

### 7.3.2 Leg imaging

Sample results of ASL data acquired during exercise are shown in **figure 7.22**. The images are of very poor quality, and this was difficult to improve. The biggest problem was the large ring-shaped artifacts around the interface between the tibia and the

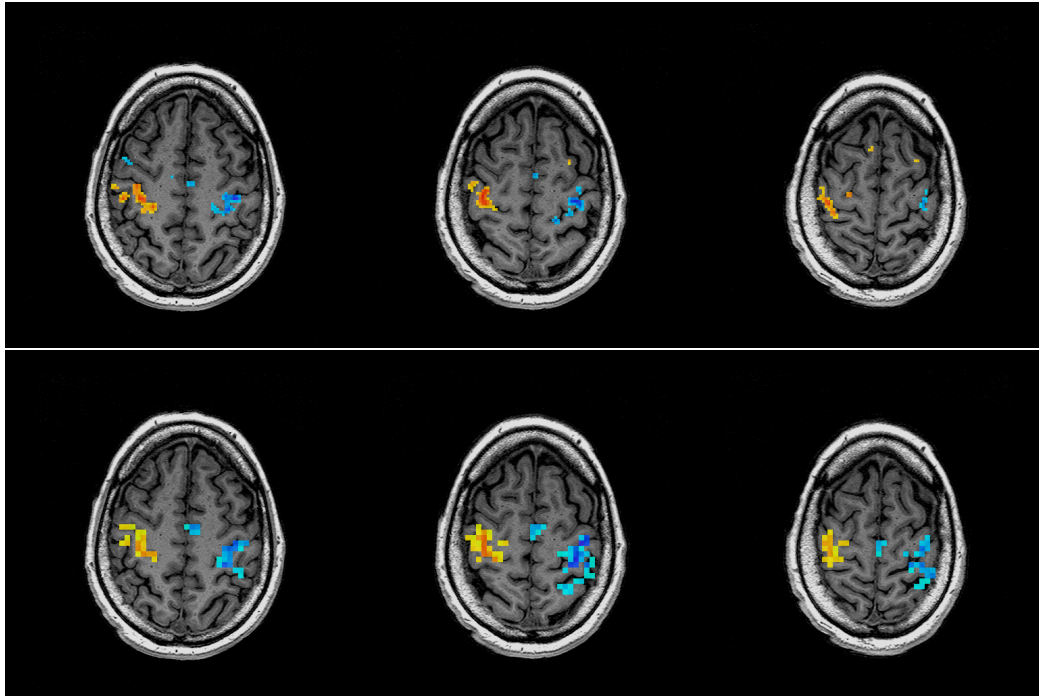


**Figure 7.21: Functional imaging of alternating hand motor task.** Thresholded correlation coefficient maps of **(top)** ASL data and **(bottom)** BOLD data. The underlay is a  $T_1$ -weighted SPGR anatomical image, acquired during the same scan session. Note that the BOLD map is  $64 \times 64$ , while the ASL is  $128 \times 128$ , because of the reconstruction procedure.

tissue. This caused areas of alternating high and low signal to permeate the signal of the muscle, thereby decreasing the SNR. The blurring artifacts are very problematic, because the scale is larger than the muscles of the lower leg. This means that signal from one muscle will be blurred throughout the image, and affect the signal in other muscles.

Nevertheless, the large ring artifacts around the tibia did subtract out to leave only smaller ring artifacts, as shown on the right of **figure 7.22**. ROI analysis was attempted on the data, with initially promising results (not shown). This analysis was abandoned when, upon closer inspection of the subtraction images, it became clear that the images contained artifacts related to the venous outflow of blood after the contractions. **Figure 7.23** shows the time series of images after a vigorous dynamic plantar flexion exercise. The arteries show an artifact consistent with circular flow patterns within the vessels (Gatehouse and Firmin 1999). Although the artifacts associated with the arteries remain relatively constant, signal dropout is evident due

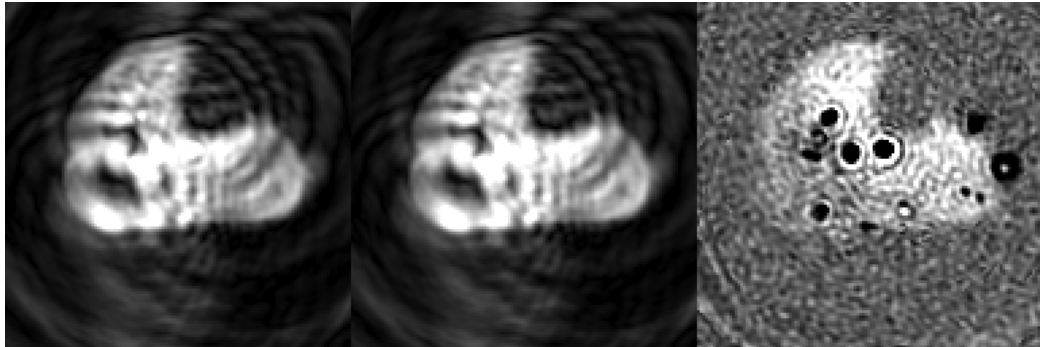


**Figure 7.22: ASL leg images.** From left to right, the unlabelled, labelled, and subtraction images from an ASL scan of the lower leg. The labelled and unlabelled images look identical, but include pervasive ring artifacts, especially around the tibia. The subtraction image has artifacts around the three arteries of the lower leg, as well as several smaller vessels.

to the veins in and around the medial gastrocnemius. The signal dropout becomes very severe along the top row of images, and then gradually subsides as the time-series continues. The artifacts nearly completely obscure the medial gastrocnemius, as well as portions of the soleus muscle.

## 7.4 Conclusions

Although the sequence was found to produce the expected results in brain imaging, artifacts associated with the spiral acquisition prevented the ASL sequence from producing reliable data in the leg. One likely reason for successful ASL in brain but not leg was thought to be due to the receiver coil. The eight channel head coil offers far superior SNR and performance compared to the single channel flex coil used for legs. The benefit of the eight individual receivers is demonstrated in **figure 7.24**. The figure shows the eight individual receiver channel images used to generate one unlabelled time-point of the ASL data. Although the resultant image shows few artifacts, the individual images display ring-shaped blur artifacts similar to those in the leg data. The artifacts are especially prominent near the sinuses, a well-known source of susceptibility effects. An eight channel coil should be built for imaging the lower legs to mitigate the effects of the off-resonant spins.

Another possible reason for poorer performance of ASL in the leg is the fact that shimming on a leg, which is cylindrical and asymmetric, is more difficult than on the head, which is spherical and symmetric (Hu et al. 1995). Use of higher order shimming (HOS) may improve the images in this case. As noted in section 2.4.2,

the spiral reconstruction includes  $B_0$  field-maps generated using the first and second echoes of the sequence, which have differing  $T_E$  by 1 ms. The field-maps were not able to correct some of the worst image artifacts produced during the spiral scans. One reason may be that phase images used to generate the field-maps included the artifacts as well, meaning that the phase data in areas that most needed correction was likely of little value. This is illustrated in **figure 7.25**, which shows the field-map of the leg. The image shows a rapidly varying field at the bone-tissue interface of the tibia. Several blurred rings surround the susceptibility artifact, just as in the magnitude images. The field-maps generated by this sequence are also problematic because of the echo spacing of 1 ms. Since the fat-water phase shift is a confound to producing  $B_0$  field-maps, the echo spacing should be carefully chosen to keep the same fat-water phase in both images. To accomplish this, the  $\Delta T_E$  should be a multiple of the inverse of the fat-water frequency difference ( $1/(440 \text{ Hz})=2.27 \text{ ms}$  at 3 T).

Finally, an inherent weakness in the ASL technique is that it requires two images to be collected in order to generate one subtraction image. If bulk motion occurs between the two acquisitions, which are separated in time by seconds, the misregistration of the fibres may cause significant artifacts. The muscle deformation associated with plantar flexion is illustrated using a special motion encoding sequence in **figure 7.26**. Given the highly non-linear and heterogeneous nature of the muscle translation during contraction, small motions during the scan could have been detrimental.

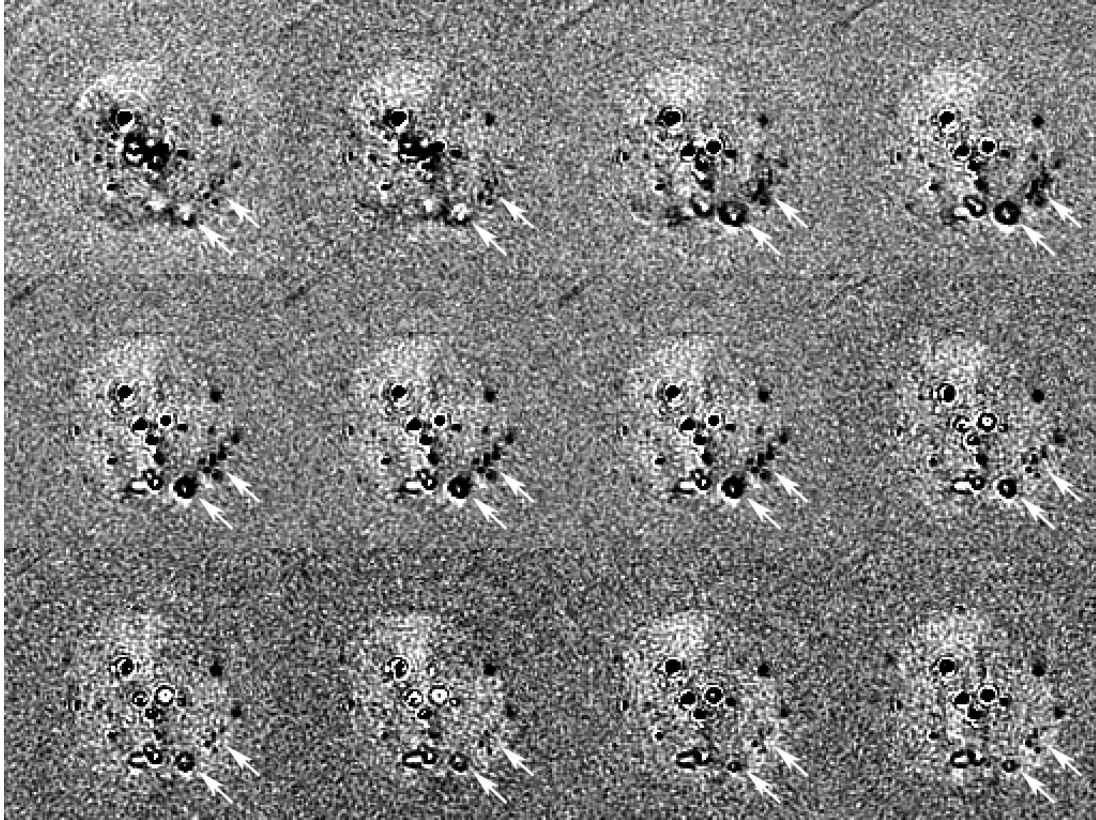


**Figure 7.23: ASL susceptibility artifact from venous outflow.** The subtraction images shown were acquired immediately after vigorous dynamic plantar flexion exercise. Time increases from left to right starting in the top left corner, with each time step being 8 seconds. The image series shows an increase in artifacts around the veins of the medial gastrocnemius (white arrows) immediately after exercise, which gradually subside.

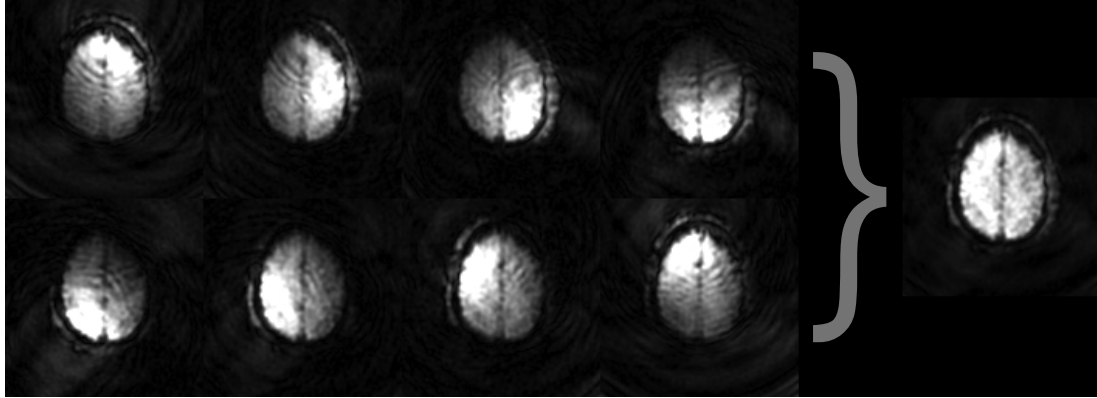


**Figure 7.24: Single coil images.** At left are the images generated from each of the eight receiver coils, and on the right is the resultant image after RMS addition.

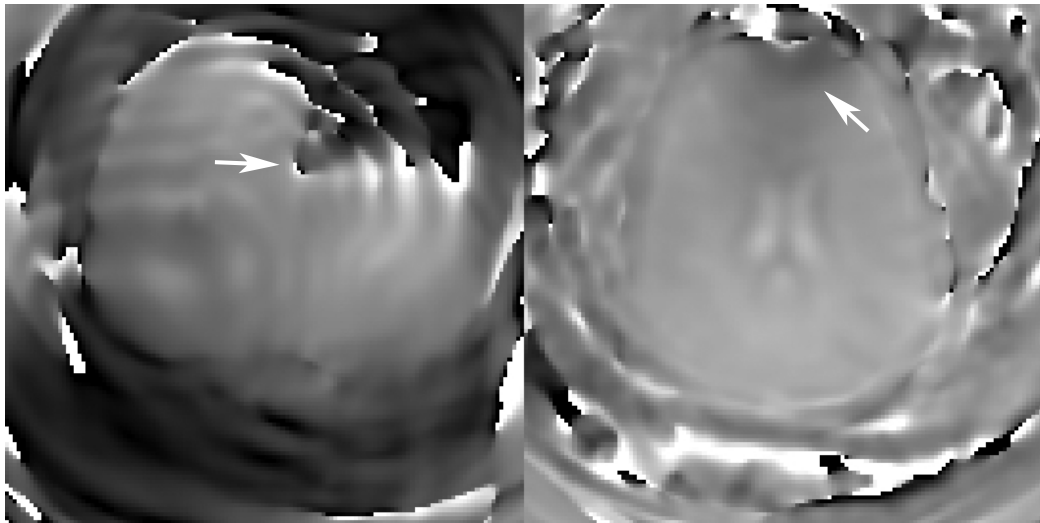


**Figure 7.25: Fieldmaps from leg and brain.**  $\Delta B_0$  maps generated from the phase data of the first two echoes of spiral ASL acquisitions. **Left:** leg data from the same series as figure 7.22, showing high inhomogeneity near the lateral edge of the tibia (white arrow), with ring artifacts around the inhomogeneity. **Right:** brain data from one receiver in the same series as figure 7.24, showing a slight inhomogeneity near the front of the brain (white arrow), likely caused by the air-tissue interface of the sinuses.

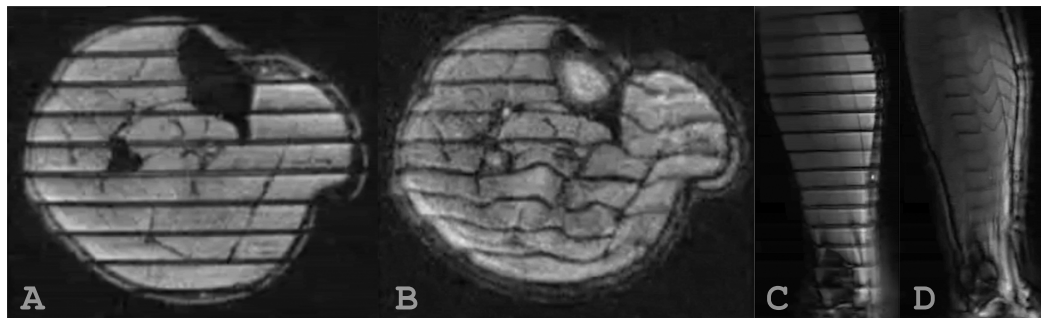


**Figure 7.26: Muscle deformation in plantar flexion.** Plantar flexion of the calf at 100% MVC is illustrated using a motion encoding sequence (Nagarsekar et al. 2009). (A) and (B) are axial images before and after contraction, respectively. (C) and (D) are sagittal images before and after contraction, respectively.



# Chapter 8

## Conclusions and future work

The acquisition of BOLD data during exercise was investigated, and motion was found to be a major confound to the measurement. Although a somewhat sophisticated motion correction scheme was developed, the BOLD data was found to be unreliable under such circumstances. The EPI and spiral BOLD data acquisition techniques were compared in the lower leg during exercise. The EPI was found to have small geometric distortions and was unreliable as a multi-shot technique. The single-shot EPI, however, outperformed even a two interleaved spiral in-out in terms of SNR and signal variability.

The ASL sequence was found to give reliable data for brain functional imaging; however, the spiral acquisition of the sequence led to artifacts that prevented signal analysis when the technique was applied to the lower leg. Although there are several potential causes for the artifacts, off-resonant effects almost certainly played a role. The effects can be mitigated by the use of a multi-channel coil.

Two ergometers were built in the course of this project to limit the motion of the exercising subject to a single plane and standardize the force. Several exercise protocols were investigated, including isometric and dynamic contractions. The protocols were probably too complex, however, which hampered physiological interpretation of the resulting BOLD signals.

### 8.1 Arterial spin labelling improvements

The first task for the future will be to build an eight receiver-channel coil for leg imaging. As demonstrated in section 7.4, the additional channels can overcome the off-resonance artifacts associated with the spiral acquisition, and lead to an overall improvement in SNR. This will allow the acquisition of higher quality ASL data, which can be used to interpret the BOLD data. The combined ASL and BOLD techniques have been used to derive the cerebral metabolic rate of oxygen consumption

(Buxton 2002). Once both methods are producing robust results in the lower leg, it should be possible to adapt the technique and calculate the metabolic rate of oxygen consumption in muscle.

There is some question about the quantification of the FAIR signal, given that the technique is somewhat sensitive to arterial transit times. A new pulse sequence can be written to improve on the current method, with a good candidate being a pulse sequence based on quantitative imaging of perfusion using a single subtraction (QUIPSS). QUIPSS uses saturation pulses before the image acquisition to control the location of the labelled blood and lessen the sensitivity to transit times (Wong et al. 1998). Another improvement on the current technique would be the addition of a large, bipolar gradient immediately before image acquisition. This would de-phase any fast moving spins and lessen the artifacts associated with flow. The addition of background suppression and the use of higher order shimming may improve the images as well. Finally, a spin echo acquisition may be prudent for the ASL sequence to eliminate any chance of influence by the BOLD effect. The sequence would likely use an EPI k-space trajectory, although fast low-angle shot (FLASH) has shown promising results as well (Wiesmann et al. 1998; Gatehouse and Firmin 1999).

### 8.1.1 BOLD-ASL interleaved imaging

The ASL pulse sequence used in this project has the capability to perform interleaved BOLD and FAIR ASL imaging. The sequence uses a spiral k-space acquisition, and alternates the BOLD scans with the labelled and control images of the ASL scan. The repeating sequence of acquisitions is BOLD-labelled-BOLD-control.

This technique is potentially useful because it acquires the BOLD and ASL data as close as possible to one another, eliminating the potential pitfalls associated with the repeatability of the exercise paradigm. Unfortunately, the interleaved sequence also decreases the time resolution of the ASL sequence by a factor of two. Since the spiral acquisition already requires two shots to get an acceptable quality image, the interleaved sequence takes at least 16 seconds to acquire a perfusion image. This represents too little information to adequately describe the post-exercise re-perfusion curve, which may take less than 30 seconds. For this reason, the BOLD-ASL interleaved sequence was not used in this project.

An alternate method has been used by Duteil et al. (2006), which purports to acquire the BOLD signal from the average image of the pulsed ASL labelled and unlabelled images:

$$BOLD = \frac{(PASL+) + (PASL-)}{2} \quad (8.25)$$

This technique seems worth pursuing, to alleviate the need to degrade the ASL temporal resolution with the interleaved BOLD images.

## 8.2 Myoglobin spectroscopy

Myoglobin spectroscopy is a relatively simple proton spectroscopic technique that can be implemented with existing hardware. At 3T, the deoxymyoglobin signal is sufficiently separated from the water peak that it can be excited and acquired directly, without water suppression (Lebon et al. 1998a; Carlier et al. 2006). This technique would complement the functional imaging methods with an independent measure of muscle oxygenation.

## 8.3 Optical methods

Near infrared spectroscopy (NIRS) has been used to monitor physiological changes in muscle (Boushel et al. 2001). The technique allows the acquisition of the ratio of oxyHb to deoxyHb, as well as total haemoglobin, or blood volume. The proposed new receiver coil should be built to incorporate NIRS optical probes, for simultaneous acquisition of this data.

With the combination of the ASL and NIRS techniques, the three major contributors to BOLD signal changes (perfusion, oxygenation, blood volume) could be measured independently. This will be invaluable for the interpretation of the BOLD signal.

## 8.4 Development of protocol and normal data

A second ergometer was designed and constructed (mostly by Dr. Bareket Falk and Raffy Dotan, Brock University, Department of Physical Education and Kinesiology), as shown in figure 8.27. The ergometer uses a pulley system with a hanging basket to provide resistance. Lead masses were added to the basket to vary the force required, which allows the administration of a one repetition maximum (1RM) test to determine the force of the subject's MVC. For the 1RM test, the resistance was increased in several steps until the subject was no longer able to perform the flexion, while vocal encouragement was given (Gibson and Noakes 2004). This measurement was confirmed with repeated tests, and a predetermined percentage of the maximum was used for the contraction intensity during scanning sessions. Several percentages were examined, for example 25%, 50%, and 75%, allowing examinations below, near, and above the threshold of contraction induced ischemia, respectively (Wigmore et al. 2004).

The use of this ergometer will continue, although likely with a simpler protocol of two percentages. A single sustained contraction to exhaustion may also be a valuable test, given the recent publication of BOLD data under a single bout of



**Figure 8.27: Pulley Ergometer.** The ergometer features a pulley system connected to a weight load to vary the contraction force.

ischemia (Potthast et al. 2009). Research ethics approval has been obtained for a study comparing children and adults during exercise, using the BOLD and ASL techniques. This study will be commenced as early as possible, as it will allow the acquisition of a normal data set for later comparison.

#### 8.4.1 New ergometer

An MRI compatible Lode cycle ergometer has been ordered (Lode B.V., Groningen, Netherlands). The ergometer features dynamic adjustment of the subject's power output during the scan session. The ergometer is made to exercise the muscles of the thigh. This may reduce motion artifacts, as rotation of the leg at the hip will not be possible when the femur is secured for scanning. A similar ergometer (installed at The Hospital for Sick Children, Toronto, ON, Canada) is pictured in **figure 8.28**.



**Figure 8.28: Lode ergometer.** The MRI compatible ergometer allows dynamic power adjustment.

## 8.5 Goal

The success of this project could lead to a test that is much more accurate for determining the stage and location of peripheral vascular disease. Even if this aspect of the project is unsuccessful, the combination of the three techniques (perfusion, oxygenation, and BOLD data) will lead to improved understanding of muscle physiology during exercise, muscle development, and the nature of the BOLD effect in muscle.



# Appendix A

## Motion correction shell script

This project involved the generation of a large number of Bourne-again shell (BASH) scripts to facilitate the data reconstruction and analysis. One such script, which may be of use to the reader, is presented here. The script uses the FLIRT linear registration tool from the FSL package to perform motion correction (<http://www.fmrib.ox.ac.uk/fsl/flirt>). This provides the use of the FLIRT weighting scheme, which allows the user to specify areas that should be registered preferentially using binary or floating point masks. The script also allows the use of three or five degrees of freedom in 2D. Lines ending with a ‘#’ character have been broken to fit the page.

```
#!/bin/bash

#-----
# This script uses flirt for motion correction, which enables -refweight, 3 or 5 DOF,
# and applying mcflirt transformation matrices, frame-by-frame
# Based on flirt_mc.sh, found on the FSL support forum
#
# v1.0 -- Mar 2009 |--| Andrew Davis -- addavis@gmail.com
#-----

printUsage() {
cat << EOF

$(basename $0)
-----
This script uses flirt for motion correction. Each volume is co-registered to a reference scan.

Usage: $(basename $0) -in inFile [options]

Options:
-in inFile      : basename for the data input
-out outFile    : basename for the data output -- default 'inFile-mc'
-ref ref        : reference for coregistration (frame number or file -- default frame 2 of inFile)
-dof n          : degrees of freedom -- default 3 (3, 5, 6, 7, 9, 12)
-cost func      : cost function -- normcorr (default), corratio, mutualinfo, normmi, leastsq
-refmask mask   : weighting mask for the reference image (mask image, thr, bet)
-inmask mask    : weighting mask for the input image (thr, bet)
-sm fwhm        : use smoothing with fwhm given here prior to coregistration
-rot_tol n      : angle for all 3 axis that is used for the search -- default 5
```

```

    -ip ip          : interpolation -- default trilinear (trilinear, nearestneighbour, sinc)
    -init          : use transformation matrix of previous volume to initialize the following
    -final         : coregister mean image of motion corrected series
    -keep          : keep temporary files when finished
    -resample      : resamples volumes to the size of the reference image
    -rsmpl_hdr file : resamples data to image size given by this header file (ignores -resample)
    -applymats dir : apply transformation matrices generated by mcflirt, and found in dir
    -use_mcflirt   : use mcflirt to generate initial transformations from smoothed data
                   (use with -sm, but -refmask, -inmask, dof are ignored with -use_mcflirt)

EOF
}

if [ $# -eq 0 ]; then printUsage; exit 1; fi # must have at least inFile

# Defaults
maskThresh=15
dof=3
rotTol=5
costFunc="normcorr"
ref=2
ip="trilinear"
sincwd=5
smoothFWHM=0

# Parse arguments
while [ $# -gt 0 ]; do
case $1 in
    -in          ) inFile=$(remove_ext $2); shift;;
    -out         ) outFile=$2; shift;;
    -ref         ) ref=$2; shift;;
    -dof         ) dof=$2; shift;;
    -cost        ) costFunc=$2; shift;;
    -refmask     ) refmask=$2; doRefmask=1; shift;;
    -inmask     ) inmask=$2; doInmask=1; shift;;
    -sm          ) smoothFWHM=$2; shift;;
    -rot_tol    ) rotTol=$2; shift;;
    -ip          ) ip=$2; shift;;
    -init        ) doInit=1;;
    -final       ) doFinalReg=1;;
    -keep        ) keepTemp=1;;
    -resample    ) doResample=1;;
    -rsmpl_hdr   ) resampleHeader=$2; doHeader=1; shift;;
    -applymats  ) applyMats=1; mcfMatDir=$2; shift;;
    -use_mcflirt) useMcflirt=1; applyMats=1;;
    *           ) echo "$(basename $0) -- Error: unrecognized option '$1'"; printUsage; exit 1;;
esac
shift
done

if [ ! "$inFile" ]; then
printUsage
exit 1
fi

if [ ! "$outFile" ]; then
outFile="${inFile}-mc"
fi

if [ $doHeader ] && [ ! -e "${resampleHeader}" ]; then
echo "$(basename $0) -- Error: reference header '$resampleHeader' not found"

```

```

    exit
fi

# Create temp and transformation matrix directories
tmpDir="${outFile}-flirt_mc-temp"
if [ -d "$tmpDir" ]; then rm -r "$tmpDir"; fi
mkdir "$tmpDir"

matDir="${outFile}.mat"
if [ -d "$matDir" ]; then rm -r "$matDir"; fi
if [ ! $applyMats ]; then mkdir "$matDir"; fi

# split 4D data into series of 3D volumes and list them
echo "Splitting 4D file..."
fslsplit "$inFile" "${tmpDir}/frame_" -t
frameList=$(basename $(ls -1 "${tmpDir}"/frame_*))

# Reference image
refFile="${tmpDir}/ref"
if [ $useMcflirt ] && [ $smoothFWHM != 0 ]; then
echo "Applying gaussian blur..."
fslmaths "$inFile" -kernel gauss $(echo "scale=2;$smoothFWHM/2.35" | bc) -fmeanu #
"${inFile}-smooth.nii.gz"

if [ -e "$ref" ]; then
fslmaths "$ref" -kernel gauss $(echo "scale=2;$smoothFWHM/2.35" | bc) -fmeanu "$refFile"
refString="-reffile $refFile"
else
refString="-refvol $ref"
fi
elif [ $useMcflirt ]; then
echo "$(basename $0) -- Error: no point in calling '-use_mcflirt' without '-sm'"
exit 2
else
if [ -e "$ref" ]; then
imcp "$ref" "$refFile"          # copy reference into temp directory
else
fslroi "$inFile" "$refFile" "$ref" 1 # extract reference volume
fi

if [ $smoothFWHM != 0 ]; then
fslmaths "$refFile" -kernel gauss $(echo "scale=2;$smoothFWHM/2.35" | bc) -fmeanu "$refFile"
fi

# Weightning mask
refWeight="${tmpDir}/refmask"
if [ $doRefmask ]; then
if [ -e "$refmask" ]; then
imcp "$refmask" "$refWeight"
else
case "$refmask" in
thr) fslmaths "$refFile" -thrp $maskThresh "$refWeight";;
bet) bet "$refFile" "${refFile}_bet" -o -m
imcp "${refFile}_bet_mask" "$refWeight";;
*) echo "ERROR: Unknown option '$refmask' for reference weightning"
exit 1;;
esac
fi
fi

inWeight="${tmpDir}/inmask"

```

```

fi

# Prepare the arguments to the flirt command call
flirtOptions="-cost $costFunc"
if [ $useMcflirt ]; then
    flirtOptions="$flirtOptions -2D -schedule $FSLDIR/etc/flirtsch/sch2D_3dof" # so slices aren't
else
    # lost off the z-axis
if [ $dof = "3" ]; then
    flirtOptions="$flirtOptions -2D -schedule $FSLDIR/etc/flirtsch/sch2D_3dof"
elif [ $dof = "5" ]; then
    flirtOptions="$flirtOptions -2D -schedule $FSLDIR/etc/flirtsch/sch2D_5dof"
else
    flirtOptions="$flirtOptions -searchcost $costFunc -searchrx -$rotTol $rotTol #
-searchry -$rotTol $rotTol -searchrz -$rotTol $rotTol"
    flirtOptions="$flirtOptions -dof $dof"
fi

if [ $doRefmask ]; then
    flirtOptions="$flirtOptions -refweight $refWeight"
fi
if [ $doInmask ]; then
    flirtOptions="$flirtOptions -inweight $inWeight"
fi
fi

echo "Calling flirt with options '$flirtOptions'..."

# Run mcflirt if desired
if [ $useMcflirt ]; then
    mcflirt -in "${inFile}-smooth.nii.gz" $refString -mats -plots
    mcfMatDir="${inFile}-smooth_mcf.mat"
    mv "${inFile}-smooth_mcf.par" "${outFile}_mcf.tsv"
fi

# Run flirt on each volume
initString=""
mcFrameList=""
matrixList=""
frameCount=1

printf "Processing $(fslval $inFile dim4)frames:"
for thisFrame in $frameList; do
    printf " $frameCount"

thisFrame="${thisFrame%.gz}" # remove extensions
thisFrame="${thisFrame%.nii}"

    if [ $smoothFWHM != 0 ]; then
        fslmaths "${tmpDir}/${thisFrame}" -kernel gauss $(echo "scale=2;$smoothFWHM/2.35" | bc) #
        -fmeanu "${tmpDir}/sm_${thisFrame}"
    fi

# Create a weighting mask for the current input
if [ $doInmask ]; then
    case "$inmask" in
        thr) fslmaths "${tmpDir}/${thisFrame}" -thrp $maskThresh "$inWeight";;
        bet) bet "${tmpDir}/${thisFrame}" "${tmpDir}/${thisFrame}_bet" -o -m
            immv "${tmpDir}/${thisFrame}_bet_mask" "$inWeight";;
        *) echo "ERROR: Unknown option '$inmask' for input weighting!"
            exit;;
    esac
fi

```

```

fi

if [ $applyMats ]; then
    matNum="${thisFrame#frame_}"
    flirt -in "${tmpDir}/${thisFrame}" -ref "${tmpDir}/${thisFrame}" -out #
"${tmpDir}/mc_${thisFrame}" -applyxfm -init "${mcfMatDir}/MAT_${matNum}" $flirtOptions
    elif [ $smoothFWHM != 0 ]; then
        flirt -in "${tmpDir}/sm_${thisFrame}" -ref "$refFile" -omat "${matDir}/${thisFrame}" #
$flirtOptions $initString
        flirt -in "${tmpDir}/${thisFrame}" -ref "$refFile" -out "${tmpDir}/mc_${thisFrame}" #
-applyxfm -init "${matDir}/${thisFrame}" $flirtOptions
    elif [ $doHeader ]; then
        flirt -in "${tmpDir}/${thisFrame}" -ref "$refFile" -omat "${matDir}/${thisFrame}" #
$flirtOptions $initString
        flirt -in "${tmpDir}/${thisFrame}" -ref "$resampleHeader" -out "${tmpDir}/mc_${thisFrame}" #
-applyxfm -init "${matDir}/${thisFrame}"
    elif [ $doResample ]; then
        flirt -in "${tmpDir}/${thisFrame}" -ref "$refFile" -omat "${matDir}/${thisFrame}" #
$flirtOptions $initString
        flirt -in "${tmpDir}/${thisFrame}" -ref "$refFile" -out "${tmpDir}/mc_${thisFrame}" #
-applyxfm -init "${matDir}/${thisFrame}"
    else
        flirt -in "${tmpDir}/${thisFrame}" -ref "$refFile" -out "${tmpDir}/mc_${thisFrame}" #
-omat "${matDir}/${thisFrame}" $flirtOptions $initString
    fi

    mcFrameList="$mcFrameList ${tmpDir}/mc_${thisFrame}"
    matrixList="$matrixList ${matDir}/${thisFrame}"

    if [ $doInit ]; then
        initString="-init ${matDir}/${thisFrame}" # initialize each frame with previous frame's
        fi # transformation matrix
done
echo ""

echo "Merging motion corrected frames..."
fslmerge -t "${outFile}" $mcFrameList

# Register mean image of motion corrected data to $refFile
if [ $doFinalReg ]; then
    fslmaths "${outFile}" -Tmean "${tmpDir}/final_mean"
    bet "${tmpDir}/final_mean" "${tmpDir}/final_mean_bet" -o -m
    inWeight="${tmpDir}/final_mean_bet_mask"

    flirt -in "${tmpDir}/final_mean" -ref "$refFile" -omat "${tmpDir}/final_mean.mat" $flirtOptions

    declare -a frames=( $frameList ) # array
    frameCount=0
    mc2FrameList=""
    for thisMatrix in $matrixList; do
        thisFrame=$(basename "${frames[$frameCount]}")
        echo "$frameCount $thisFrame $thisMatrix mc2_${thisFrame}"
        convert_xfm -omat "$thisMatrix" -concat "$thisMatrix" "${tmpDir}/final_mean.mat"
        flirt -in "${tmpDir}/${thisFrame}" -ref "${tmpDir}/final_mean" -o "${tmpDir}/mc2_${thisFrame}" #
-omit "$thisMatrix" $flirtOptions -applyxfm
        mc2FrameList="$mc2FrameList ${tmpDir}/mc2_${thisFrame}"
        ((frameCount++))
    done

    fslmerge -t "${outFile}" $mc2FrameList

```

```
fi

# Generate motion correction parameters
#fsl_mcpair $outFile.mat -corr -out ${outFile}.par

# Clean up
if [ ! $keepTemp ]; then rm -r "$tmpDir"; fi

if [ $useMcflirt ]; then
rm -r "${inFile}-smooth.nii.gz" "${inFile}-smooth_mcf.nii.gz" "${inFile}-smooth_mcf.mat"
fi
```

# Glossary

**atherosclerosis**

a disease characterized by narrowed arteries; 5

**bandwidth**

a range of frequencies; 8

**collateral circulation**

blood supplied indirectly from a distant artery; 5

**dorsalis pedis artery**

the artery along the back of the foot; 6

**dorsiflexion**

movement of the foot towards the shin; 4

**embolus**

blood clot or other particle that migrates through the vessels and becomes lodged in a thinner section; 5

**endogenous**

occurring naturally within the body; 20

**ergometer**

tool to quantify applied forces or energy during muscle contraction; 30

**eversion**

motion away from the midline of the body; 4

**femoral artery**

artery that runs down the medial side of the thigh; 5, 6

**Fourier transform**

mathematical tool to convert between frequency and spatial domains; 7

**gangrene**

tissue death due to insufficient blood flow. The dry form causes withering of the tissue, whereas the wet form involves bacterial infection; 5

**gradient coils**

MRI scanner components that produce variable magnetic fields across the volume of interest, for spatial localization as well as specialized applications such as motion encoding; 8

**hypertension**

blood pressure above that which is considered normal for a particular age group; 5

**intermittent claudication**

pain in the legs or feet when walking, which is relieved by resting; 5

**ischemia**

reduced blood flow to an area of tissue; 5

**k-space**

the co-ordinate system into which raw MRI data is read before it is Fourier transformed; 9

**lateral**

away from the vertical midline of the body; 3

**magnetization**

the extent to which the individual magnetic dipoles of a material align with an external field; 7

**medial**

toward the vertical midline of the body; 3

**perfusion**

blood supply; 20

**plantar flexion**

movement of the foot away from the shin; 3

**popliteal artery**

artery running along the back of the knee; 6

**posterior tibialis artery**

the artery running under the lower medial protuberance of the tibia; 6

**precession**

rotational motion of a vector about another axis; 7

**pulse sequence**

program of gradient lobes and RF pulses that determines the image character;  
6

**registration**

alignment of image geometry across scans or subjects; 32

**renal**

related to the kidneys; 6

**shimming**

using dedicated scanner gradients to cause the main magnetic field to be as homogeneous as possible; 15

**slew rate**

(of the gradients:) maximum rate of change of gradient amplitude; 16

**spiral**

k-space trajectory for fast image acquisition; 15

**stenosis**

abnormal narrowing of the arteries; 6

**supine**

laying on one's back; 6

**systolic blood pressure**

peak blood pressure; 6

**thrombus**

blood clot on a vessel wall that tends to impede blood flow; 5

**transverse plane**

plane perpendicular to the main magnetic field; 8

**voxel**

volume element of a 3D image; 10



# Bibliography

- Abul-Khoudoud, O. 2006. "Diagnosis and risk assessment of lower extremity peripheral arterial disease." *J Endovasc Ther* 13(Suppl 2): II10–18.
- Ahmed, N. 2005. "Advanced glycation endproducts—role in pathology of diabetic complications." *Diabetes Res Clin Pract* 67: 3–21.
- Ahn, C., J. Kim, and Z. Cho. 1986. "High-speed spiral-scan echo planar NMR imaging—I." *IEEE transactions on medical imaging* MI-5: 2–7.
- Bernstein, M. A., K. F. King, and X. J. Zhou. 2004. *Handbook of MRI Pulse Sequences*. Amsterdam: Elsevier, Inc.
- Block, K. T. and J. Frahm. 2005. "Spiral imaging: a critical appraisal." *J Magn Reson Imaging* 21: 657–68.
- Boslaugh, S. and P. A. Watters. 2008. *Statistics in a Nutshell: A Desktop Quick Reference*. Sebastopol, California: O'Reilly Media, Inc.
- Boss, A., P. Martirosian, C. D. Claussen, and F. Schick. 2006. "Quantitative ASL muscle perfusion imaging using a FAIR-TrueFISP technique at 3.0 T." *NMR in biomedicine* 19: 125–32.
- Boushel, R., H. Langberg, J. Olesen, J. Gonzales-Alonzo, J. Bülow, and M. Kjaer. 2001. "Monitoring tissue oxygen availability with near infrared spectroscopy (NIRS) in health and disease." *Scandinavian journal of medicine & science in sports* 11: 213–22.
- Bulte, D. P., J. Alfonsi, S. Bells, and M. D. Noseworthy. 2006. "Vasomodulation of skeletal muscle BOLD signal." *J Magn Reson Imaging* 24: 886–90.
- Bulte, D. P., S. Bells, and M. D. Noseworthy. 2004. "Nicotine induced changes in muscle BOLD signal at 3T." *Proceedings of the International Society for Magnetic Resonance in Medicine* 12: 1036.

- Buxton, R. B. 2002. *Introducion to Funcional Magnetic Resonance Imaging: Principles & Techniques*. New York: Cambridge University Press.
- Carlier, P. G., D. Bertoldi, C. Baligand, C. Wary, and Y. Fromes. 2006. "Muscle blood flow and oxygenation measured by NMR imaging and spectroscopy." *NMR in biomedicine* 19: 954–67.
- Cox, R. W. 1996. "Afni: software for analysis and visualization of functional magnetic resonance neuroimages." *Comput Biomed Res* 29: 162–73.
- Damon, B. M., J. L. Hornberger, M. C. Wadington, D. A. Lansdown, and J. A. Kent-Braun. 2007a. "Dual gradient-echo MRI of post-contraction changes in skeletal muscle blood volume and oxygenation." *Magn Reson Med* 57: 670–9.
- Damon, B. M., M. C. Wadington, J. L. Hornberger, and D. A. Lansdown. 2007b. "Absolute and relative contributions of BOLD effects to the muscle functional MRI signal intensity time course: effect of exercise intensity." *Magn Reson Med* 58: 335–45.
- de Bazelaire, C. M. J., G. D. Duhamel, N. M. Rofsky, and D. C. Alsop. 2004. "MR imaging relaxation times of abdominal and pelvic tissues measured in vivo at 3.0 T: preliminary results." *Radiology* 230: 652–9.
- Detre, J. A. and J. Wang. 2002. "Technical aspects and utility of fMRI using BOLD and ASL." *Clinical neurophysiology* 113: 621–34.
- Duteil, S., C. Wary, J. S. Raynaud, V. Lebon, D. Lesage, A. Leroy-Willig, and P. G. Carlier. 2006. "Influence of vascular filling and perfusion on BOLD contrast during reactive hyperemia in human skeletal muscle." *Magn Reson Med* 55: 450–4.
- Eiberg, J. P., G. Madycki, M. A. Hansen, S. Christiansen, J. B. G. Rasmussen, and T. V. Schroeder. 2002. "Ultrasound imaging of infrainguinal arterial disease has a high interobserver agreement." *Eur J Vasc Endovasc Surg* 24: 293–9.
- Frank, L. R., E. C. Wong, L. J. Haseler, and R. B. Buxton. 1999. "Dynamic imaging of perfusion in human skeletal muscle during exercise with arterial spin labeling." *Magn Reson Med* 42: 258–67.
- Gatehouse, P. D. and D. N. Firmin. 1999. "Flow distortion and signal loss in spiral imaging." *Magn Reson Med* 41: 1023–31.
- Gibson, A. S. C. and T. D. Noakes. 2004. "Evidence for complex system integration and dynamic neural regulation of skeletal muscle recruitment during exercise in humans." *Br J Sports Med* 38: 797–806.

- Glover, G. 1999. "Simple analytic spiral k-space algorithm." *Magn Reson Med* 42: 412–415.
- Glover, G. H. and C. S. Law. 2001. "Spiral-in/out BOLD fMRI for increased SNR and reduced susceptibility artifacts." *Magn Reson Med* 46: 515–22.
- Gold, G. E., E. Han, J. Stainsby, G. Wright, J. Brittain, and C. Beaulieu. 2004. "Musculoskeletal MRI at 3.0 T: relaxation times and image contrast." *AJR Am J Roentgenol* 183: 343–51.
- Haacke, E. M., R. W. Brown, M. R. Thompson, and R. Venkatesan. 1999. *Magnetic Resonance Imaging: Physical Principles and Sequence Design*. Hoboken, NJ: John Wiley & Sons, Inc.
- Hardy, C. and H. Cline. 1989. "Broadband nuclear magnetic resonance pulses with two-dimensional spatial selectivity." *J Appl Phys* 66: 1513–16.
- Hashemi, R. H. and J. W. G. Bradley. 1997. *MRI: The Basics*. Baltimore, Maryland: Lippincott Williams & Wilkins.
- Hlushchuk, Y. and R. Hari. 2006. "Transient suppression of ipsilateral primary somatosensory cortex during tactile finger stimulation." *J Neurosci* 26: 5819–24.
- Hu, J., T. Javaid, F. Arias-Mendoza, Z. Liu, R. McNamara, and T. R. Brown. 1995. "A fast, reliable, automatic shimming procedure using  $^1\text{H}$  chemical-shift-imaging spectroscopy." *J Magn Reson B* 108: 213–9.
- Irrazabal, P., C. H. Meyer, D. G. Nishimura, and A. Macovski. 1996. "Inhomogeneity correction using an estimated linear field map." *Magn Reson Med* 35: 278–82.
- Jezzard, P. and R. S. Balaban. 1995. "Correction for geometric distortion in echo planar images from  $B_0$  field variations." *Magn Reson Med* 34: 65–73.
- Katsilambros, N., E. Dounis, P. Tsapogas, and N. Tentolouris. 2003. *Atlas of the Diabetic Foot*. Hoboken, NJ: John Wiley & Sons, Inc.
- Kim, S. G. 1995. "Quantification of relative cerebral blood flow change by flow-sensitive alternating inversion recovery (FAIR) technique: application to functional mapping." *Magn Reson Med* 34: 293–301.
- Kim, S. G., N. V. Tsekos, and J. Ashe. 1997. "Multi-slice perfusion-based functional MRI using the FAIR technique: comparison of CBF and BOLD effects." *NMR in biomedicine* 10: 191–6.

- King, K. F., A. Ganin, X. J. Zhou, and M. A. Bernstein. 1999. "Concomitant gradient field effects in spiral scans." *Magn Reson Med* 41: 103–12.
- Klarhöfer, M., M. Barth, and E. Moser. 2002. "Comparison of multi-echo spiral and echo planar imaging in functional MRI." *Magn Reson Imaging* 20: 359–64.
- Koziak, A. M., J. Winter, T.-Y. Lee, R. T. Thompson, and K. S. S. Lawrence. 2008. "Validation study of a pulsed arterial spin labeling technique by comparison to perfusion computed tomography." *Magnetic resonance imaging* 26: 543–53.
- Labs, K. H., M. R. Nehler, M. Roessner, K. A. Jaeger, and W. R. Hiatt. 1999. "Reliability of treadmill testing in peripheral arterial disease: a comparison of a constant load with a graded load treadmill protocol." *Vascular medicine* 4: 239–46.
- Lebon, V., C. Brillault-Salvat, G. Bloch, A. Leroy-Willig, and P. G. Carlier. 1998a. "Evidence of muscle BOLD effect revealed by simultaneous interleaved gradient-echo NMRI and myoglobin NMRS during leg ischemia." *Magn Reson Med* 40: 551–8.
- Lebon, V., P. G. Carlier, C. Brillault-Salvat, and A. Leroy-Willig. 1998b. "Simultaneous measurement of perfusion and oxygenation changes using a multiple gradient-echo sequence: application to human muscle study." *Magn Reson Imaging* 16: 721–9.
- Ledermann, H. P., H.-G. Heidecker, A.-C. Schulte, C. Thalhammer, M. Aschwanden, K. A. Jaeger, K. Scheffler, and D. Bilecen. 2006a. "Calf muscles imaged at BOLD MR: correlation with TcPO<sub>2</sub> and flowmetry measurements during ischemia and reactive hyperemia—initial experience." *Radiology* 241: 477–84.
- Ledermann, H.-P., A.-C. Schulte, H.-G. Heidecker, M. Aschwanden, K. A. Jäger, K. Scheffler, W. Steinbrich, and D. Bilecen. 2006b. "Blood oxygenation level-dependent magnetic resonance imaging of the skeletal muscle in patients with peripheral arterial occlusive disease." *Circulation* 113: 2929–35.
- Li, T.-Q., A. Takahashi, Y. Wang, V. Mathews, and G. H. Glover. 2006. "Dual-echo spiral in/in acquisition method for reducing magnetic susceptibility artifacts in blood-oxygen-level-dependent functional magnetic resonance imaging." *Magn Reson Med* 55: 325–34.
- Ljunggren, S. 1983. "A simple graphical representation of fourier-based imaging methods." *J Magn Reson* 54: 338–343.

- Look, D. C. and D. R. Locker. 1970. "Time saving measurements of NMR and EPR relaxation times." *Rev Sci Instrum* 41: 250–251.
- Mansfield, P. 1977. "Multi-planar image formation using NMR spin echoes." *Journal of Physics C: Solid State Physics* 10: L55–L58.
- Marcovitch, H., ed. 2005. *Black's Medical Dictionary*. 41st edition. London: A & C Black.
- Marieb, E. N. and K. Hoehn. 2010. *Human Anatomy & Physiology*. 8th edition. Toronto: Benjamin Cummings.
- McRobbie, D. W., E. A. Moore, M. J. Graves, and M. R. Graves. 2006. *MRI; From Picture to Proton*. 2nd edition. New York: Cambridge University Press.
- Merli, G., H. Weitz, and R. Anthony, eds. 2004. *Peripheral Vascular Disorders: Management in Primary Care*. Amsterdam: Elsevier, Inc.
- Meyer, C., B. Hu, and D. Nishimura. 1992. "Fast spiral coronary artery imaging." *Magn Reson Med* 28: 202–213.
- Meyer, R., K. K. McCully, R. W. Reid, and B. Prior. 2001. "BOLD MRI and NIRS detection of transient hyperemia after single skeletal muscle contractions." *Proceedings of the International Society for Magnetic Resonance in Medicine* 9: 135.
- Meyer, R. A., T. F. Towse, R. W. Reid, R. C. Jayaraman, R. W. Wiseman, and K. K. McCully. 2004. "BOLD MRI mapping of transient hyperemia in skeletal muscle after single contractions." *NMR in biomedicine* 17: 392–8.
- Muir, R. L. 2009. "Peripheral arterial disease: Pathophysiology, risk factors, diagnosis, treatment, and prevention." *Journal of vascular nursing* 27: 26–30.
- Nagarsekar, G., J. Hodgson, D. Shin, and S. Sinha. 2009. "Development of a spin tag sequence with spiral acquisition for elucidating shear at the deep gastrocnemius aponeurosis and other dynamics of the musculoskeletal elements of the lower leg." *Proceedings of the International Society for Magnetic Resonance in Medicine* 17: 549.
- Nishimura, D. G., P. Irarrazabal, and C. H. Meyer. 1995. "A velocity k-space analysis of flow effects in echo-planar and spiral imaging." *Magn Reson Med* 33: 549–56.
- Noseworthy, M. D., D. P. Bulte, and J. Alfonsi. 2003. "BOLD magnetic resonance imaging of skeletal muscle." *Seminars in musculoskeletal radiology* 7: 307–15.

- Nygren, A. T. 2006. "Shortened T2 after exercise in ischemic skeletal muscle." *J Magn Reson Imaging* 23: 177–82.
- Ogawa, S., T. M. Lee, A. S. Nayak, and P. Glynn. 1990. "Oxygenation-sensitive contrast in magnetic resonance image of rodent brain at high magnetic fields." *Magn Reson Med* 14: 68–78.
- Peräkylä, T., H. Tikkanen, J. von Knorring, and M. Lepäntalo. 1998. "Poor reproducibility of exercise test in assessment of claudication." *Clinical physiology* 18: 187–93.
- Potthast, S., A. Schulte, S. Kos, M. Aschwanden, and D. Bilecen. 2009. "Blood oxygenation level-dependent MRI of the skeletal muscle during ischemia in patients with peripheral arterial occlusive disease." *Rofo* 181: 1157–61.
- Price, T. B., G. Kamen, B. M. Damon, C. A. Knight, B. Applegate, J. C. Gore, K. Eward, and J. F. Signorile. 2003. "Comparison of MRI with EMG to study muscle activity associated with dynamic plantar flexion." *Magn Reson Imaging* 21: 853–61.
- Robson, M. D., A. W. Anderson, and J. C. Gore. 1997. "Diffusion-weighted multiple shot echo planar imaging of humans without navigation." *Magn Reson Med* 38: 82–8.
- Roemer, P. B., W. A. Edelstein, C. E. Hayes, S. P. Souza, and O. M. Mueller. 1990. "The NMR phased array." *Magn Reson Med* 16: 192–225.
- Sangill, R., M. Wallentin, L. Østergaard, and P. Vestergaard-Poulsen. 2006. "The impact of susceptibility gradients on cartesian and spiral EPI for BOLD fMRI." *Magma* 19: 105–14.
- Schulte, A.-C., M. Aschwanden, and D. Bilecen. 2008. "Calf muscles at blood oxygen level-dependent MR imaging: aging effects at postocclusive reactive hyperemia." *Radiology* 247: 482–9.
- Seeley, R., T. Stephens, and P. Tate. 2004. *Anatomy and Physiology*. 6th edition. McGraw-Hill.
- Smith, S. M., M. Jenkinson, M. W. Woolrich, C. F. Beckmann, T. E. J. Behrens, H. Johansen-Berg, P. R. Bannister, M. D. Luca, I. Drobnjak, D. E. Flitney, R. K. Niazy, J. Saunders, J. Vickers, Y. Zhang, N. D. Stefano, J. M. Brady, and P. M. Matthews. 2004. "Advances in functional and structural MR image analysis and implementation as FSL." *Neuroimage* 23 Suppl 1: S208–19.

- Stanisz, G. J., E. E. Odrobina, J. Pun, M. Escaravage, S. J. Graham, M. J. Bronskill, and R. M. Henkelman. 2005. "T1, t2 relaxation and magnetization transfer in tissue at 3T." *Magn Reson Med* 54: 507–12.
- Takahashi, A., T.-Q. Li, and H. Stødkilde-Jørgensen. 1997. "A pulse sequence for flow evaluation based on self-refocused RF and interleaved spiral readout." *J Magn Reson* .
- Tan, H., J. Anderson, H. Woldeyesus, C. M. Kramer, and C. H. Meyer. 2008. "High resolution ASL and BOLD imaging in skeletal muscle using spiral sequences." *Proceedings of the International Society for Magnetic Resonance in Medicine* 16: 2576.
- Towse, T., J. Slade, J. Ambrose, M. DeLano, and R. Meyer. 2009. "Quantitative analysis of the post-contractile BOLD effect in human skeletal muscle." *Proceedings of the International Society for Magnetic Resonance in Medicine* 17: 547.
- Towse, T. F., J. M. Slade, and R. A. Meyer. 2005. "Effect of physical activity on MRI-measured blood oxygen level-dependent transients in skeletal muscle after brief contractions." *J Appl Physiol* 99: 715–22.
- Vlaardingerbroek, M. T. and J. A. den Boer. 2003. *Magnetic Resonance Imaging: Theory and Practice*. 3rd edition. Berlin: Springer-Verlag.
- Walker, W. F. 1980. *A Colour Atlas of Peripheral Vascular Diseases*. Smeets-Weert, Holland: Wolfe Medical Publications, Ltd.
- Wang, D., W. Strugnell, G. Cowin, D. M. Doddrell, and R. Slaughter. 2004. "Geometric distortion in clinical MRI systems part I: evaluation using a 3D phantom." *Magn Reson Imaging* 22: 1211–21.
- Wiesmann, F., P. D. Gatehouse, J. R. Pantiing, A. M. Taylor, D. N. Firmin, and D. J. Pennell. 1998. "Comparison of fast spiral, echo planar, and fast low-angle shot MRI for cardiac volumetry at .5T." *J Magn Reson Imaging* 8: 1033–9.
- Wigmore, D. M., B. M. Damon, D. M. Pober, and J. A. Kent-Braun. 2004. "MRI measures of perfusion-related changes in human skeletal muscle during progressive contractions." *J Appl Physiol* 97: 2385–94.
- Williams, D. S., J. A. Detre, J. S. Leigh, and A. P. Koretsky. 1992. "Magnetic resonance imaging of perfusion using spin inversion of arterial water." *Proc Natl Acad Sci USA* 89: 212–6.
- Wong, E. C., R. B. Buxton, and L. R. Frank. 1998. "Quantitative imaging of perfusion using a single subtraction (QUIPSS and QUIPSS II)." *Magn Reson Med* 39: 702–8.

- Woolrich, M. W., S. Jbabdi, B. Patenaude, M. Chappell, S. Makni, T. Behrens, C. Beckmann, M. Jenkinson, and S. M. Smith. 2009. "Bayesian analysis of neuroimaging data in FSL." *Neuroimage* 45: S173–86.
- Wu, W.-C., J. Wang, J. A. Detre, F. W. Wehrli, E. Mohler, S. J. Ratcliffe, and T. F. Floyd. 2008a. "Hyperemic flow heterogeneity within the calf, foot, and forearm measured with continuous arterial spin labeling MRI." *Am J Physiol Heart Circ Physiol* 294: H2129–36.
- Wu, W.-C., J. Wang, P. Wang, J. A. Detre, T. Olufade, and T. F. Floyd. 2008b. "Continuous arterial spin labeling in progressive peripheral vascular disease." *Proceedings of the International Society for Magnetic Resonance in Medicine* 16: 3676.
- Yang, Y., G. H. Glover, P. van Gelderen, A. C. Patel, V. S. Mattay, J. A. Frank, and J. H. Duyn. 1998. "A comparison of fast MR scan techniques for cerebral activation studies at 1.5 tesla." *Magn Reson Med* 39: 61–7.
- Ziegler-Graham, K., E. J. MacKenzie, P. L. Ephraim, T. G. Trivison, and R. Brookmeyer. 2008. "Estimating the prevalence of limb loss in the united states: 2005 to 2050." *Arch Phys Med Rehabil* 89: 422–9.